Capturing Cell Dynamics in Live Pancreatic Adenocarcinoma

A Thesis

SUBMITTED TO THE FACULTY OF

THE UNIVERSITY OF MINNESOTA

BY:

Nelson J. Rodríguez Merced

IN PARTIAL FULFILLMENT OF THE REQUIREMENTS

FOR THE DEGREE OF MASTER OF SCIENCE

ADVISOR:

Dr. Paolo P. Provenzano

January 2020

Acknowledgements

I would like to express my deepest gratitude to my advisor Dr. Paolo P. Provenzano for the opportunity he gave me to conduct research under his guidance and support which, both professionally and personally, made all this work possible. I deeply appreciate his passion and dedication to this work and his support on my professional/personal career goals. He is one of my greatest advocates and has pushed me to strive further, overachieve goals and made me into a better engineer and scientist.

I would like to thank my fellow lab mates for their friendship, continuous help and support through my research. Thanks for being available to bounce ideas and learn new techniques from each one of you. Also, thanks for being my family away from home. All of you have shown me the value of teamwork and dedication that I will take with me throughout my career. Mackenzie, thanks for your availability to talk through any issues, both personal and professional. Your overall support, and our collaborations, encouraged me to move forward and grow no matter the obstacles that may come up. Rachel E., thanks for being an example in the lab of hard work and dedication. You inspire me to never give up and continue following my dreams. Rachel H., thanks for your challenging questions, which were necessary to develop a scientific mindset and approach to the experiments performed, and for teaching me the ropes on many lab techniques. Ethan, Jon and Kenneth, thanks for your availability and help with purchasing, lab operation, lab maintenance, mouse colony monitoring, and among other things, not only for me but for the whole lab. Dr. Kianna Elahi-Gedwillo, thanks for helping me feel part of the group and for sharing your knowledge and experiences even in the short time we worked together. Dr. Arja Ray, thanks for your support and for allowing me to collaborate on several projects. They served as an exceptional introduction to the lab environment and to develop the various skills I required to perform my studies. Dr. Ajay Dixit, thanks for your friendship and your availability to share your knowledge with me. Dr. Amanda Salzwedel, thanks for your mentorship from my time as your intern, in 2016, till today as your labmate. Dr. Erdem Tabdanov, thank you for your willingness to share your resources, knowledge and to collaborate on multiple projects. These have, without a doubt, allowed me to significantly grow and expand my knowledge as a scientist.

I would like to thank my best friend, Carlos Colon, for always being available to hear me out, support me through anything and cheering me up. I would like to thank my mother and father, grandparents, who have always supported me and challenged me to strive further, surpassing set goals, and to be a better professional and person. There are not enough words to describe my gratitude for all their continued sacrifices. I would also like to give special thanks to my wife Rocio Del Mar Mendez Peña for her love, support, and for always pushing me towards a better version of myself. She was always willing to hear my crazy ideas, plans and positive/negative outcomes while caring for me through any challenging times. Her willingness to support me from afar falls short in illustrating our love and support for one another. With all of this said, thanks again to all mentioned, and everyone who, in one way or another, helped to mold me into a better scientist, professional and person.

Dedication

I would like to dedicate this work to my grandparents Jose L. Merced Alvarez, Gladys Perez Tirado, my parents Nelson F. Rodriguez Figueroa, Elizabeth Merced Perez and my amazing wife Rocio Del Mar Mendez Peña. All whom, through hard work, love and support, pushed me to excel in all of my endeavors.

Abstract

Pancreatic ductal adenocarcinoma (PDA) is one of the most aggressive and lethal cancers and is associated with a robust fibroinflammatory stromal response termed desmoplastic reaction. This stromal response causes the local microenvironment to significantly aid disease progression by providing drug free sanctuaries, immunosuppressive niches, and suppressing cytotoxic T lymphocyte infiltration and distribution, due in part to the increased intra-tumoral pressure and robust extracellular matrix proteins (ECM) density. In order for $CD8^+$ cytotoxic T cells to infiltrate and eliminate cancer cells, they need to migrate efficiently through the dense tumor microenvironment (TME). Thus, altering external (ECM content/architecture) and internal (modulating microtubule (MT) dynamics in immune cell) factors has the potential to enhance efficient infiltration of native or engineered cytotoxic T lymphocytes so they effectively sample the tumor volume to combat disease. Therefore, to analyze the infiltration capabilities in a dense tumor environment, we optimized an approach to culture live tumor slices over 1-4 days in order to perform live cell imaging of carcinoma and immune cell dynamics in complex TMEs with nonlinear optical imaging platforms. From human peripheral blood or tumor-bearing mouse model of PDA, $CD4^+$ or $CD8^+$ cytotoxic T lymphocytes, respectively, were isolated, activated, labeled and later introduced to 3D collagen matrices and live murine PDA tumor slice explants, which has a complex multi-cellular environment and contains elements of the original TME and architecture. Furthermore, we used CRISPR technology to engineer T cells to lack GEF-H1 and alter MT→GEF-H1→RhoA pathway to determine its effect on cell motility. We employed two-photon excitation and second harmonic generation (SHG) imaging to visualize cell dynamics and ECM architecture, and quantify T cell migration behavior through 3D collagen matrices and the native PDA tumor architectures. To test approaches to re-engineer TMEs, we are specifically altering ECM composition and architecture in PDA and quantifying changes in T cell behavior. Thus, combined, these live measures and quantitative analysis will form the basis for our understanding of cell migration in the complex microenvironment and set the mark for our objective to modulate immunity in tumors.

Table of Contents

List of Figures

Chapter 1. Introduction

Chapter 3. Tumor Slice Culture and Imaging as a Tool to Visualize Live Tumor Dynamics

Chapter 4. Modulating Disease Response with STT

Chapter 5. Enhancing T Cell Migration Through Structurally and Mechanically Complex Tumor Microenvironments

Appendix B

List of Videos

Movie 1: Live imaging of mCD8+ T cells (green) migrating in liver slices containing PDA metastasis (red) from *KPCT* mouse. Carcinoma cells can be seen actively migrating along collagen fibers (cyan). Time lapse images are maximum intensity projections (MIPs) of a 50 µm z-stack.

Movie 2: Maximum intensity projection of 75µm z-stack of a time-lapse sequence of mCD8+ T cells (green) migrating along aligned collagen (cyan) in live liver slices with metastasis (red). mCD8+ T cells can be seen migrating along aligned collagen fibers.

Movie 3: Live imaging of *KPC* tumor slices, stained with celltracker red with collagen pseudo colored cyan, treated with 0.5mg/mL collagenase for 30 min. Imaging started within 5 min of treatment. Time lapse images are MIPs of a 75 µm z-stack.

Movie 4: Live imaging of *KPC* tumor slices, stained with celltracker red with collagen pseudo colored cyan, treated with 100U/mL hyaluronidase for 30 min. Imaging started within 5 min of treatment. Time lapse images are MIPs of a 75 µm z-stack.

Movie 5: Live imaging of mCD8+ T cells (green) migrating along *KPCT* tumor slices (carcinoma cell red) with collagen (cyan) for 45 min. Time lapse images are MIPs of a 75 µm z-stack.

Movie 6: Live imaging of mCD8+ T cells (green) migrating along 3D collagen matrices (grey) for 45 min. Time lapse images are MIPs of a 75 µm z-stack.

Movie 7: Live imaging of mCD8+ T cells (green) migrating along *KPCT* tumor slices (tdTomato+ carcinoma cells red) with collagen (cyan). Time lapse images are MIPs of a 75 µm z-stack.

Movie 8: Live imaging of mCD8+ T cells (green) migrating along *KPC* tumor slices (stained with celltracker red) with collagen (cyan) for 45 min. Time lapse images are MIPs of a 75 µm z-stack.

List of Abbreviations

ECM: extracellular matrix

HA: Hyaluronan

KPC: *Kras$_{G12D/+}$;p53$_{R172H/+}$;Pdx1-Cre* (genetically-engineered mouse model)

KPCT: *Kras$_{G12D/+}$;p53$_{R172H/+}$;Pdx1-Cre;ROSA$_{Tdtomato/+}$* (fluorescent reporter *KPC* model)

MT: microtubule

PanIN: pancreatic intraepithelial neoplasm (preinvasive stage of PDA)

PDA: pancreatic ductal adenocarcinoma

SHG: second harmonic generation

STT: stroma-targeted therapy

TACS: tumor associated collagen signatures

TME: tumor microenvironment

Chapter 1. Introduction

1.1 Pancreatic Ductal Adenocarcinoma (PDA)

1.1.1 Survival statistics and standard of care

Pancreatic ductal adenocarcinoma (PDA) is one of the most aggressive and lethal cancers. The estimated incidence of pancreatic cancer in 2019 was 56,770 new cases with 45,750 deaths while the 5-year survival is ~9%, the lowest among all cancers (Siegel et al., 2019). These statistics are due, in part, to the lack of early detection and unique characteristics within PDA microenvironment (e.g. fibrotic and immunosuppressive stroma) which renders current treatments (e.g. chemotherapies, radiotherapies and immunotherapies) ineffective (Kaur et al., 2012). Gemcitabine, a palliative chemotherapeutic, has been primarily used to treat advanced cases of PDA (Burris et al., 1997). Over time, marginal improvements in PDA treatment have been achieved using FOLFIRINOX (Conroy et al., 2011), which is a chemotherapy regimen made up of four drugs, and, more recently, nab-Paclitaxel in combination with gemcitabine has now become the new standard of care for metastatic PDA (Goldstein et al., 2015). Besides the obvious need for new diagnostic techniques for early detection of PDA, in order to treat the disease rather than its symptoms, novel approaches to dismantle PDA tumor microenvironment (TME) and activate the immune system is required.

1.1.2 Models of PDA

Several models have been proposed to study PDA such as cell lines, 2-3D cultures, xenografts and organoids but they fail to replicate the native and complex heterogeneity of PDA (Behrens et al., 2017; Hwang et al., 2016). Genetically engineered mouse models (GEMMs) of PDA, which faithfully recapitulate key processes observed in human disease (Elahi-Gedwillo et al., 2019; Hingorani et al., 2005; Provenzano et al., 2012), have been used as a valuable preclinical model for human disease for studying pancreatic tumorigenesis, gene alterations and evaluation of therapies (Behrens et al., 2017). Recently, culturing tumor slices, from human tumors and mouse models (e.g. GEMMs) (Davies et al., 2015), has emerged as a novel model that faithfully recapitulates the complex interactions in the TME between carcinoma cells, the immune system, and the stroma,

which is considered a target for fine tuning PDA treatments (Jiang et al., 2017; Misra et al., 2019; Vennin et al., 2018). Thus, using GEMMs and patient tumor slices will help in shaping our understanding of the TME and will potentially generate novel ideas to overturn cancer progression.

1.1.3 Stroma targeted therapies (STT) in PDA

The ECM is a complex macromolecular network composed of distinctive physical, biochemical, and biomechanical properties and components, such as collagen, hyaluronans (HA), fibronectins, proteoglycans, glycoproteins and laminins which provide structural support for cells and tissues (Lu et al., 2012; Raglow and Thomas, 2015). The ECM is also physiologically active, and responsible for cell–cell communication, cell adhesion, cell proliferation (Walker et al., 2018) and contains cytokines, growth factors, and hormones secreted by cells (Wang et al., 2017). When dysregulated, it is a driving factor for fibrotic diseases and cancer, including metastasis (Cox and Erler, 2011). Disease advancement and progression, via metastasis, are aided by highly aligned ECM or collagen known as tumor associated collagen signatures (TACS) (Provenzano et al., 2008a; Ray et al., submitted). It has been reported in several studies that highly aligned TACS, perpendicular to tumor boundary (TACS-3), are negative prognostic factors in various cancers such as breast (Conklin et al., 2011) and PDA (Drifka et al., 2016).

T cell migration into and within tumors is guided by chemokines and ECM proteins (Franciszkiewicz et al., 2012; Friedl and Weigelin, 2008). ECM structures can provide a scaffold that supports 3D T cell migration, but dense ECM fiber alignment can create nonpermissive matrix regions that exclude T cells while switching their migrational mode from chemokine to stroma guided migration, misdirecting them from their migration towards tumor cells (Hartmann et al., 2014). Several studies have demonstrated such nonpermissive stromal areas in human tumors, which may complicate antitumor immune responses (Ohno et al., 2002; Peranzoni et al., 2013; Salmon et al., 2012a).

PDA microenvironment is associated with robust fibrotic and immunosuppressive stroma which significantly aid disease progression by providing drug free sanctuaries, immunosuppressive niches (Clark et al., 2007; Stromnes et al., 2014), aligned ECM (I.e.

collagen) highways for metastasis (Ray et al., submitted), and suppressing cytotoxic T lymphocyte infiltration and distribution (Clark et al., 2007; Elahi-Gedwillo et al., 2019), due in part to the increased intra-tumoral pressure and robust ECM density (e.g. collagen and HA) (Provenzano et al., 2012). This stromal complexity of PDA, starts to develop from preinvasive PanIN stage to invasive stage, contributing to the unique pathology of PDA (**Fig. 1**). During this process, α-SMA+ myofibroblasts begin to populate the pancreas microenvironment around early stage PanIN lesions and persist throughout later stages of disease (**Fig. 1A-C**), depositing a robust ECM network (**Fig. 1D-L**). This ECM network consists largely of collagen matrix (**Fig. 1D-F**), confirmed to be largely fibrillar collagen from SHG (**Fig. 1G-I**) and known to contribute to cancer cell dissemination in PDA (Ray et al., submitted), as well as large quantities of hyaluronan (**Fig. 1J-L**), contributing to grossly elevated interstitial fluid pressure (IFP) in PDA (**Fig. 1T**) (Provenzano et al., 2012). Elevated IFP hinders small molecule drug delivery as they may have to be transported against pressure gradient which will also contribute to the collapse of blood vessels from preinvasive PanIN disease to advanced PDA (**Fig. 1M-O, S**), limiting drug delivery (Provenzano et al., 2012).

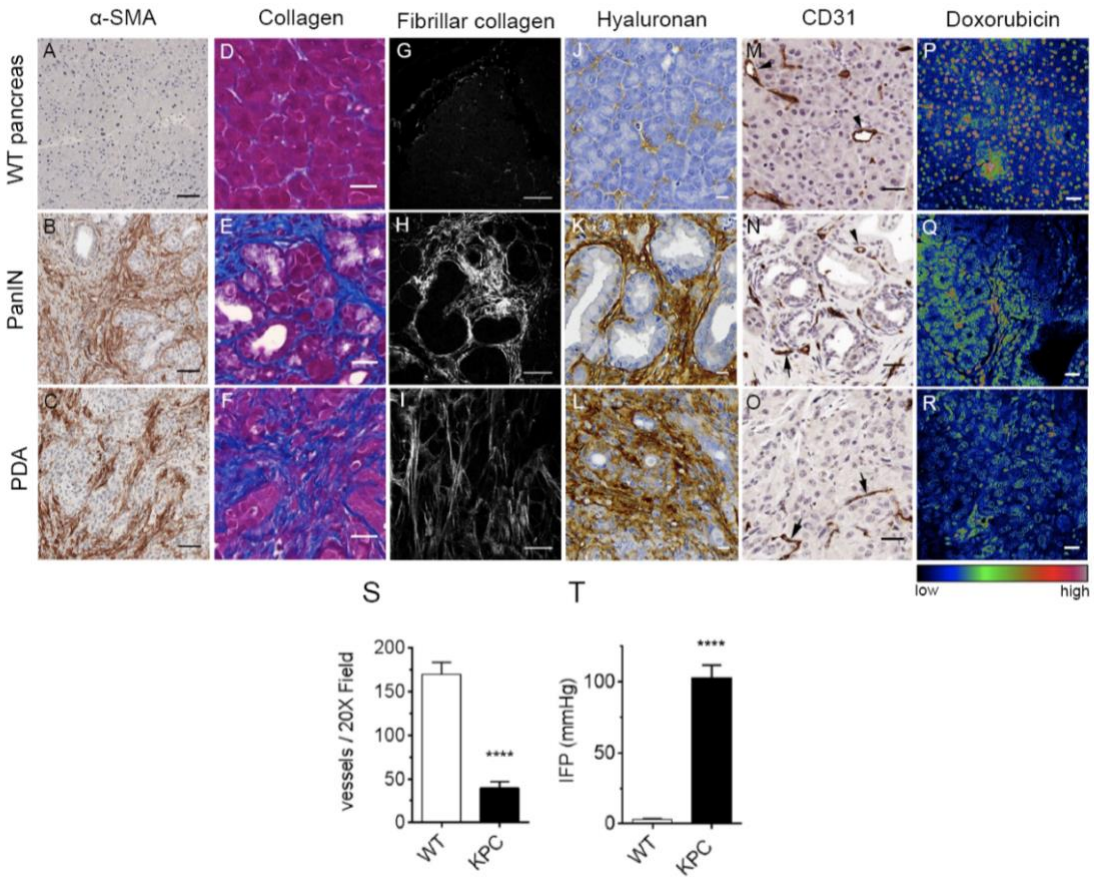

Figure 1: Desmoplasia during disease progression in PDA. (**A-C**) There is a high density of α-SMA+ myofibroblasts that emerge during PanIN stages and remain prevalent throughout PDA. (**D-F**) Masson's trichrome staining shows increasing collagen deposition by myofibroblasts as disease progresses. (**G-I**) Stromal collagen is primarily fibrillar, as imaged using second harmonic generation. (**J-L**) Likewise, the glycosaminoglycan, hyaluronan, increases in density with disease progression. (**M-O**) Immunohistochemical staining of CD31 shows the transition from open, patent blood vessels in normal, wildtype (WT) pancreas (arrowheads) to increasingly nonfunctional, collapsed blood vessels (arrows). (**P-R**) The effects of increased ECM deposition and decreased vascular functionality have a strong impact on distribution capabilities of small molecules, such as doxorubicin (color scalebar 0-255 for low to high signal). (**S**) PDA exhibits a striking lack of vasculature compared to WT pancreas. (**T**) The robust desmoplastic response in PDA leads to extremely elevated interstitial fluid pressure (IFP) in the tumor space. Scale bar = 25 μm. ****p-value < 0.0001. *Figure used with permission: Elahi-Gedwillo et al., 2019, Cancer Res.* (Elahi-Gedwillo et al., 2019).

Several studies suggest that disrupting these ECM proteins and stromal cell function, with stroma targeted therapies (STT), either directly or indirectly, with collagenase (Salmon et

al., 2012b), PEGPH20 (Jacobetz et al., 2013; Provenzano et al., 2012), Halofuginone (Elahi-Gedwillo et al., 2019), losartan (Chauhan et al., 2013), focal adhesion kinase inhibition (FAKi) (Jiang et al., 2016), colony-stimulating factor-1 receptor and chemokine receptor 2 inhibitors (Mitchem et al., 2013), chemokine ligand 12 inhibitor (Feig et al., 2013) and CD40 agonist (Beatty et al., 2011) have provided multiple benefits. These benefits are: decreasing intratumoral pressure while opening vasculature (improving drug distribution), break down ECM architecture or metastatic paths, due to antifibrotic effect, reverses immunosuppression and can be cytotoxic to the tumor. Several of these STTs are currently being tested in the clinic with promising results (e.g. PEGPH20 (Hingorani et al., 2017), Losartan (Murphy et al., 2019), and FAKi (NCT02546531). Thus, therapeutic strategies to re-engineer TMEs, to move them toward normalization, and combination strategies, with chemotherapies and immunotherapies, may have the potential to be an effective treatment strategy to treat cancers such as PDA.

1.1.4 Immune landscape in PDA

PDA is generally described as poorly immunogenic (Martinez-Bosch et al., 2018) (I.e. unable to induce a positive immune response) due to having a lower rate of mutations (Jones et al., 2008), compared to other cancers, therefore being poorly antigenic (Beatty and Gladney, 2015), and containing a highly immunosuppressive TME. At times, immune cells can make up to 50% of the tumor cell mass (Feig et al., 2012). The immunosuppressive TME of PDA is composed of Tregs, tumor-associated macrophages (TAMs) and myeloid-derived suppressor cells (MDSCs) (Martinez-Bosch et al., 2018), which accumulate even at preinvasive disease (Clark et al., 2007), and block the anti-tumoral activity of effector $CD4^+$ and $CD8^+$ T-cells (Amedei et al., 2013; Ino et al., 2013; Liyanage et al., 2002; Zhao et al., 2009). Specifically targeting these immunosuppressive cells has shown positive outcomes in treating PDA. Disruption of CCR5/CCL5 signaling blocks the migration/homing of Treg cells to tumors and inhibits pancreatic tumor growth in mice (Tan et al., 2009). Targeting TAMs improves chemotherapeutic efficacy by decreasing the number of tumor initiating cells in PDA and reactivates antitumor $CD8^+$ T cell response during chemotherapeutic treatment (Mitchem et al., 2013). Similarly,

depleting MDSCs has the ability to sensitize PDA to a positive immune response by accumulating CD8 T cells promoting tumor cell death in PDA (Stromnes et al., 2014). It may even be beneficial to target these immunosuppressive cells from their temporal inception in the TME to overcome their immunosuppressive effect (Stromnes et al., 2014). The amount of T cell infiltration is an important prognostic factor in various types of cancers (Hartmann et al., 2014). Human PDAC frequently induces an immune response resulting in marked T-cell infiltration (von Bernstorff et al., 2001; Emmrich et al., 1998; Hartmann et al., 2014). Strong infiltration, especially by cytotoxic $CD8^+$ T cells, is usually associated with improved patient outcomes (Carstens et al., 2017; Fukunaga et al., 2004; Ino et al., 2013). However, the majority of tumor-infiltrating T cells become trapped in the stroma and thus the T cells do not reach the cancer cells in sufficient numbers (von Bernstorff et al., 2001; Ryschich et al., 2005). Studies that targeted the stroma in concert with immunotherapies (checkpoint inhibition) have observed strong immune response in PDA (Feig et al., 2013; Jiang et al., 2016), demonstrating that a robust antitumor immune response can take place in PDA under the right therapeutic conditions (Elahi-Gedwillo et al., 2019). Thus, re-engineering the stroma, as mentioned above, and engineering novel ways of improving T cell migration in tumors are key to re-establishing cytotoxic T cell contact with cancerous tissue and ultimately eliminating cancers such as PDA.

Chapter 2. Materials and Methods

2.1 Cell culture

Human CD4+ (hCD4+) T cells were produced by CD4+ cell isolation and purification from the whole human blood (sex unknown), supplied by STEMCELL™ Technologies Inc., where blood was tested for Hepatitis C and HIV. CD4+ T cell isolation and purification was performed with EasySep™ Human CD4+ T Cell Isolation Kit (STEMCELL™ Technologies Inc., USA) and, and then cultured, activated and expanded in ImmunoCult™-XF T Cell Expansion Medium (STEMCELL™ Technologies Inc., USA) with the addition of ImmunoCult™ Human CD3/CD28/CD2 T Cell Activator and Human Recombinant Interleukin 2 (IL-2, STEMCELL™ Technologies Inc., USA) as per STEMCELL™ Technologies Inc. commercial protocol. These cells were provided by Dr. Erdem Tabdanov. For CRISPR protocols, hCD4+ T cells, derived from human whole peripheral blood (sex unknown), were activated and expanded using ImmunoCult™ Human CD3/CD28/CD2 T Cell Activator (STEMCELL Technologies Inc.), following the manufacturer's recommendation, in ImmunoCult™-XF T Cell Expansion Medium (STEMCELL Technologies Inc.) supplemented with Human Recombinant IL-2 (STEMCELL Technologies Inc). For CRISPR experiments, peripheral blood mononuclear cells (PBMCs) from de-identified healthy human donors were obtained using Trima Accel leukoreduction system (LRS) (Memorial Blood Centers, Minneapolis, MN). PBMCs were further purified using ammonium chloride-based red blood cell lysis and a Ficoll-Paque gradient. CD4+ T cells were isolated from the PBMC population by immunomagnetic positive selection using the MojoSort Human CD4 Nanobeads (BioLegend, San Diego, CA) and an EasySep Magnet (STEMCELL Technologies, Cambridge, MA). These cells were provided by Dr. Branden Moriarity. Mouse CD8+ T (mCD8+) were isolated from tumor bearing *KPC* or *KPCT* mice (*Kras*$^{G12D/+}$*;p53*$^{R172H/+}$*;Pdx1-Cre* or *Kras*$^{G12D/+}$*;p53*$^{R172H/+}$*;Pdx1-Cre;ROSA*$^{Tdtomato/+}$, respectively), using EasySep™ Mouse CD8+ T Cell Isolation Kit (STEMCELL Technologies Inc.) following the manufacturer's recommendation. After isolation, mCD8+ T cell activation and expansion was performed using Dynabeads Mouse T-Activator CD3/CD28 (Thermo Fisher Scientific), following the manufacturer's recommendation, in ImmunoCult™-XF T Cell Expansion Medium

supplemented with Human Recombinant IL-2 for at least 4 days. Magnetic separation was done to separate beads from cells. Cells can be used immediately or can be frozen down in freezing medium (15% DMSO in FBS) for future use. Note that frozen T cells were given an incubation/recovery period ($t \geq 24$ hours) in ImmunoCult™ expansion medium, supplied with human IL-2 after cell thawing, in order to avoid the effects of cold exposure shock. All cell work was approved by the University of Minnesota Institutional Biosafety Committee and followed institutional and NIH guidelines.

2.2 Human and mouse pancreatic tissues and tumors

Freshly resected PDA sections from the clinic were obtained from BioNet (University of Minnesota) in compliance with approved Institutional Review Board protocols. Fresh tissues were kept on ice in cell culture media for transportation, formalin-fixed immediately upon arrival and subsequently paraffin-embedded and sectioned for analysis. Genetically engineered *KPC* (*Kras*$^{G12D/+}$*;p53*$^{R172H/+}$*;Pdx1-Cre*) mice were used as a faithful mouse model for pancreatic cancer that recapitulate key processes observed in human disease (Elahi-Gedwillo et al., 2019; Hingorani et al., 2005; Provenzano et al., 2012). Pancreatic tumor samples were obtained from the *KPC* model and some of its variants (*KPCT: KPC; ROSA26*$^{LSL\text{-}tdTomato/+}$ (Elahi-Gedwillo et al., 2019), *KPCG: KPC; ROSA26*$^{LSL\text{-}ZsGreen+/+}$ (Ray et al., 2017a) or *KPCY*: *LSL-Kras*^{G12D}*; Trp53*$^{flox/+}$*; p48-Cre; LSL-YFP* (Jiang et al., 2016) with fluorophores expressed specifically in pancreatic carcinoma cells. Liver samples with metastasis were obtained from the *KPCT* model with advanced disease. All animal studies were approved by the University of Minnesota Institutional Animal Care and Use Committee.

2.3 Staining and imaging of archival tissues

Formalin-fixed paraffin-embedded (FFPE) sections were imaged on a custom-built multiphoton laser scanning microscope (Prairie Technologies / Bruker) using a Mai Tai Ti:Sapphire laser (Spectra-Physics) using simultaneous multiphoton excitation (MPE) and second harmonic generation (SHG) to visualize cells and collagen, respectively, that has been described previously (Carlson et al., 2017). This system was controlled using

PrairieView software. Samples were excited at 800 and 880nm wavelengths. To capture SHG from collagen, samples were imaged at 880nm and harmonic signal captured with a blue bandpass filter with a 440 or 450nm center wavelength. Human sections were stained with FITC-conjugated anti-pan Cytokeratin antibody to visualize carcinoma cells. Sections from *KPCY* and *KPCT* mice were additionally stained with anti-GFP antibody and anti-RFP antibody, respectively, and Alexa-conjugated secondary antibodies (Thermo Fisher) were used to visualize the YFP^+ and $tdTomato^+$ carcinoma cells post-fixation. The YFP and tdTomato fluorescence was visualized by 800 or 880nm two-photon excitation with a green and a red emission filter, respectively.

For staining FFPE sections, slides were first dewaxed and rehydrated in xylene and ethanol followed by antigen retrieval by steam heating in 1X Trilogy (Cell Marque). Slides were permeabilized with 0.025% Triton-X-100 (Roche) in 1X TBS (Bio-Rad) (TBS-T) and blocked for 1h at RT with 5% goat serum (Vector Labs) in 1X TBS-T. After blocking, slides were incubated overnight in a humidified chamber at 4 °C in TBS-T with 1% Fatty acid free-BSA (Fisher Scientific) with anti-mouse/human antibodies. The following primary antibodies were used in different experiments: 1:50 mouse anti-Cytokeratin Pan-FITC (MilliporeSigma, Human), 1:200 rat anti-mouse CD31 (Dianova, Mouse), 1:200 rabbit anti-CD31/PECAM-1 (Novus Biologicals, Human), 1:400 rabbit anti-RFP (ABCAM, Mouse), 1:200 rabbit anti-GFP (Life Technologies, Mouse). Subsequently, the slides were washed and incubated for 1h at RT with 1:200 Alexa-fluor secondary antibodies: goat anti-rabbit 488 (Life Technologies), goat anti-rat 568 (Life Technologies) along with 1:500 Draq5 (Biolegend) nuclear stain followed by wash steps and mounting with Prolong Gold (Life Technologies).

2.4 Quantification of collagen content and architecture

For unbiased quantification of collagen content and TACS, multiple SHG images were taken at random locations on several slides obtained from different *KPCT*, *KPCG* and *KPCY* mice. These images of different regions represented various grades or stages of PDA progression such as normal, adjacent normal, PanIN, undifferentiated PDA or well-differentiated PDA, which were determined by combining pathological assessment (also

in case of the human samples) and inspection of hematoxylin and eosin (H&E) stained serial sections of the same tumor (pathological assessment was performed by Dr. Arja Ray). The SHG images were then run through a custom MATLAB (The MathWorks, Inc.) code that dynamically thresholds images to retain collagen positive pixels in a binary image. Quantification of TACS-2 and TACS-3 was obtained using CurveAlign (LOCI), a freely available software that calculates the angular distribution of collagen fibers with respect to a user-defined ductal boundary (50) (analysis was performed by Dr. Arja Ray). The percentage of positive pixels were then calculated and used as a measure of fibrous collagen content (**Supplementary Fig. 1**). To obtain the frequencies of TACS-2 and TACS-3 occurrence, the total number of TACS-2+ and TACS-3+ ducts were noted and corresponding percentages obtained. Single cell extrusion events were also noted and correlated with their corresponding TACS-2 or TACS-3.

2.5 T cell genome engineering with CRISPR

Single guide RNAs (sgRNAs) were designed to hARHGEF2 using the Synthego CRISPR design tool (https://design.synthego.com/). The top two recommended guides were obtained as modified sgRNAs (Synthego, Menlo Park, CA). Both sgRNAs were screened in K562 cells and the most efficient gRNA (Sequence: 5'-GAGGUGCCCAUUGGUAUAGC -3'), based on knockout score, was used in subsequent experiments with primary human T cells (**Supplementary Figure 4A**). For T cell culture, T cells were maintained in OpTmizer CTS T cell Expansion serum-free media (SFM) containing 2.5% CTS Immune Cell Serum Replacement (SR) (ThermoFisher, Waltham, MA), L-Glutamine, Penicillin-Streptomycin, N-Acetyl-L-cysteine (10 mM), rhIL-2 (300 IU/mL), rhIL-7 (5 ng/mL), and rhIL-15 (5 ng/mL), at 37 ℃ with 5% CO_2. T cells were activated with Dynabeads Human T-Activator CD3/CD28 (ThermoFisher, Waltham, MA) at a 2:1 bead:cell ratio for 48 h prior to electroporation. T cells were maintained at ~1×10^6/mL in normal tissue culture flasks for experiments optimizing editing efficiency. For T cell electroporation, after 48 hours, Dynabeads were magnetically removed and cells were washed with PBS once prior to resuspension in appropriate electroporation buffer. 1×10^6 Primary Human T cells were electroporated using the 4D-nucleofector (Lonza,

Basel, Switzerland) and a P3 Primary Cell 4D-Nucleofector™ X Kit (V4XP-3032). 1.5 µg CleanCap Cas9 mRNA (TriLink Biotechnologies, San Diego, CA) and 1 ug of modified gRNA were added to 1×10^6 cells in 20 µL of the recommended electroporation buffer. The mixture was electroporated using the program EO-115. Cas9 mRNA alone was used as a control for all conditions. Following electroporation, T cells were allowed to recover in antibiotic-free medium at 37 °C, 5% CO2 for 20 min, then cultured in complete CTS OpTmizer T cell Expansion SFM as described above. Genomic DNA was taken from T cells 7 days post electroporation by spin column-based purification. Cas9 efficiency was analyzed on the genomic level by PCR amplification of CRISPR-targeted loci (Forward sequence: 5'- AGGGAGATGAGTGGCAACAG -3'; Reverse sequence: 5'- CAGCTGGGGATCAGAGAGAA -3'), Sanger sequencing of the PCR amplicons (Eurofins Genomics, Louisville, KY), and subsequent analysis of the Sanger sequencing traces using the ICE web app developed by Synthego (https://ice.synthego.com/). Validation and engineered Human T cell testing, preparation and culture was performed and were provided by Dr. Branden Moriarity's Lab.

2.6 Preparation of 3D collagen matrices

Collagen matrices were prepared, as previously described (Ray et al., 2017a, 2018). Briefly, high concentration rat-tail collagen I (VWR) was neutralized with a 1:1 ratio of 100 mM HEPES (Thermo Fisher Scientific) in 2X PBS and completed to a final concentration of 3 mg/mL with DMEM (Corning) supplemented with 10% FBS (which introduces fibronectin (FN). The mixture was allowed to sit in ice for 5 min, after which 350 mL was pipetted into a standard 24-well plate. The gels were left polymerizing for 20 min, in the hood, at room temperature and then incubated at 37ºC with 5% CO_2 for 3 h and subsequently overlaid with DMEM (Corning) and incubated overnight at 37ºC with 5% CO_2.

2.7 T cell migration in 3D collagen matrices

3×10^5 viable $hCD4^+$ or $mCD8^+$ cells were stained with 1 µM of CellTracker Green CMFDA (5-chloromethylfluorescein diacetate; Thermo Fisher) for 5 minutes, protected

from light, at 37ºC. Lymphocytes were centrifuged at 300 g for 5 min and washed twice in L-15 plus 1% FBS and resuspended in the same media to a volume of 200 µL. Excess overlaid media from the collagen matrices was removed completely prior to seeding T-cells. The 3×10^5 T cells in 200 µL were gently pipetted on top of the collagen matrix, gently swirled to evenly distribute the cell suspension and incubated for 30 min at 37ºC and 0% CO_2 to allow lymphocytes to infiltrate the gel matrix. After incubation, the remaining media on top of the matrix was removed and washed once to remove cells that did not infiltrate/adhere to the gel. Gel was carefully detaching from all sides using a pipette tip and transferred to a 35 mm dish using tweezers. A slice anchor (Warner Instruments) was used to hold the gel in place and was overlaid with 5 mL of L-15 media plus 1% FBS in control (DMSO), 70 nM Taxol, 10 µM Nocodazole, 5 ug/mL RhoA Activator II (Cytoskeleton, Inc.) or 2 µg/mL Rho A Inhibitor I (Cytoskeleton, Inc.) conditions and imaged immediately after designated incubation time as per commercial protocol (Cytoskeleton Inc.). Briefly, for Rho A activation or inhibition, prior to staining T cells with CMFDA, T cells were resuspended in serum free RPMI with 5 µg/mL and 2 µg/mL of activator and inhibitor for 3 and 4 hours, respectively.

2.8 Mouse slice culture

Freshly explanted *KPC* and *KPCT* tumors were harvested at endpoint and placed in ice cold sterile PBS with soybean trypsin inhibitor (STI; ATCC). 1.5% agarose (Genemate) gel was prepared and super glued (Loctite) onto the vibratome (Vibratome Company) cutting stage to create a support for the tumor which was super glued directly in front of the agarose gel. The stage was overlaid with ice cold PBS. The sectioning parameters were: speed (3 mm/s), amplitude (8 mm) and thickness (350 µm). Slices were placed in ice cold sterile PBS with STI for transport and subsequently cultured (4 days maximum), as described previously (Jiang et al., 2019) with modifications. Briefly, multiple slices were transferred, using tweezers, and placed flat on 0.4 µm, 30 mm diameter cell culture inserts (Millipore Sigma) pre-coated with collagen gel mixture, as described above but completed with 1X PBS instead of growth media, in a 6-well plate, with RPMI 1640 supplemented with 10% FBS, 1% penicillin and streptomycin, 14.5 mM Hepes, 5 µg/mL plasmocin

(Invivogen) and 10 µg/mL of STI in a 37ºC humidified incubator at 5% CO_2. Single slices can be cultured similarly in a 0.4 µm, 12 mm diameter cell culture inserts (Millipore Sigma) in a 24-well plate. The culture media was changed daily. Fixation and processing steps were done as previously described (Nagaraj et al., 2018). Liver slices were cut at a thickness of 400µm thickness and cultured similarly as tumor slices for a maximum of 2 days.

2.9 T cell migration in tumor slices

KPC Slices were transferred to a 24 well plate and cultured in L-15 media supplemented with 10% FBS, 1% penicillin and streptomycin, 5 µg/mL plasmocin and 10 µg/mL of STI with 5 µM of CellTracker Red CMTPX (Invitrogen) for 15-20 minutes at 37ºC with 0% CO_2 incubator. *KPCT* slices were not stained with CellTracker Red since carcinoma cells can be visualized via red fluorescence. Slices were washed twice in cell tracker free media. For STT studies, slices were incubated in slice culture media with 0.5 mg/mL collagenase or 100 U/mL hyaluronidase for 15 min, in 24-well plates, followed by two washes in STT free culture media. Individual tumor and liver slices were then transferred using tweezers to the 12 mm culture inserts in the 24-well plate. 1-2 x 10_5 $mCD8_+$ T cells were stained, as described above, and concentrated in 100 µL of L-15 media supplemented with 10% FBS and immediately added onto the slice, in the inserts, as to concentrate the cells on the slice and let the cells adhere/migrate on the tissue for 1 hr at 37ºC with 0% CO_2 incubator. Slices were then handled with tweezers and gently washed in the same media to remove excess T cells that did not migrate/adhered into the tissue and transferred to a 3.5 cm dish. A slice anchor was used to hold the tissue in place and immediately overlaid with 5 mL of L-15 media plus 1% FBS in control (DMSO), 70 nM Taxol and 10 µM Nocodazole conditions and imaged immediately. L-15 media supplemented with 10% FBS, 1% penicillin and streptomycin, 5 µg/mL plasmocin, 10 µg/mL of STI and 30U/mL IL-2 was used for seeding and imaging T cell migration on *KPC*/*KPCT* slices, subjected to STT, and on *KPCT* liver slices.

2.10 Multiphoton microscopy of 3D live cell imaging and analysis of 3D cell migration

Cell migration data was collected by imaging using a custom-built multiphoton laser scanning microscope (MPLSM) using a Mai Tai Ti:Sapphire laser to simultaneously generate MPE and SHG to visualize cells and collagen, respectively, at an excitation wavelength of 880 nm with a custom-built temperature-controlled stage insert, as described previously (Ray et al., 2017a, 2017b, 2018). Briefly, time-lapse imaging of T cells inside 3D collagen matrix and on tumor slices, was obtained by creating two-channel (T cells and collagen) or three-channel (T cells, collagen, and *KPC*-tissue/*KPCT*-carcinoma cells/liver-tissue) Z-stacks of 75 µm depth at 5 µm steps, at each stage position, every 1.5 min up to 45 min (for migration analysis) of imaging or longer. Five dimensions (x, y, z, t, in two/three channels) time-lapse images were post-processed in Fiji (Schindelin et al., 2012), drift corrected using 3D correction plugin (Parslow et al., 2014) and cell tracking was performed using Trackmate Plugin (Tinevez et al., 2017) in Fiji. Quantification and analysis of tracks was performed as previously described in (Ray et al., 2017a, 2017b). Briefly, cell trajectories were fit to a persistent random walk model (PRWM) (Harms et al., 2005; Othmer et al., 1987) using the method of overlapping intervals (Dickinson and Tranquillo, 1993) using MATLAB as previously described (Ray et al., 2017a).

Briefly, the mean squared displacement (MSD) for a cell over a time interval t_i was obtained by averaging all the squared displacements x_{ik} such that

$$\overline{x_i} = \frac{1}{n_i}\sum_{k=1}^{n_0} \overline{x_{ik}},$$

$$n_i = N - i + 1,$$

Where n_i is is the number of overlapping intervals of duration t_i and N is the total number of intervals. Mathematically, the persistent random walk model can be written as:

$$MSD\ (t) = 2S^2P[t - P(1 - e^{\frac{-t}{P}})],$$

Where S is the migration speed and P is the persistence time. The motility coefficient is given as:

$$\mu = \frac{S^2P}{n_d},$$

Where n_d is the dimensionality. Since the model was fit separately into the three orthogonal directions, we obtained motility, speed, and persistence times for x, y and z directions, therefore $n_d = 1$ in each case.

For total speed of each cell, we took the square root of the squared sum of each speed in the x, y and z directions as follows:

$$S = \sqrt[2]{S_x^2 + S_y^2 + S_z^2},$$

For total motility of each cell, we added the different motilities from each direction as follows:

$$\mu = \mu_x + \mu_y + \mu_z,$$

2.11 FAK inhibition in *KPC* mice

Control and FAKi samples have been previously described (Jiang et al., 2016). Briefly, 50mg/kg VS-4718 (Verastem Inc.) was administered by oral gavage twice a day in a formulation with 0.5% carboxymethyl cellulose and 0.1% Tween-80 (Sigma) in sterile inhibitor.

2.12 Atomic force microscopy

Human CD4+ T cells were plated on a glass-bottom dish (Willco Wells) pre-coated with either ICAM-1 (Life Technologies) or 0.01% poly-L-lysine (Sigma-Aldrich) and immersed in culture media solution (Life Technologies). Force spectroscopy atomic force microscopy (AFM) experiments were performed using a Bruker Bioscope Catalyst AFM system (Bruker) mounted on an inverted Axiovert 200M microscope (Zeiss) equipped with a confocal laser scanning microscope 510 Meta (Zeiss) and a 40x objective lens (0.95 NA, Plan-Apochromat, Zeiss). The hybrid microscope instrument was placed on an acoustic isolation table (Kinetic Systems). During AFM experiments, T cells were maintained at physiological relevant temperature 37ºC using a heated stage (Bruker). A soft silicon nitride tipless AFM probe (HQ:CSC38/tipless/Cr-Au, MikroMasch) was used for T cell's compression. The AFM microcantilevers were pre-calibrated using the standard thermal noise fluctuations method. The estimated spring constants for microcantilevers used were 0.07 – 0.1 N/m. After calibration, the AFM probe was moved on top of a rounded T cell.

Five to ten successive force curves were performed on each T cell. The deflection set-point was set to 20 nm yielding applied forces between 1.5 to 2 nN.

2.13 Analysis of AFM data: Determination of T cell's cellular surface tension

All AFM force-distance curves measurements were analyzed using a custom-built MATLAB code to calculate the cellular surface tension. For curves fitting, indentation depths between 0-400 nm were relatively consistent in yielding good fits (R_2>0.9). Curves with poor fits R_2<0.9 were discarded from the analysis. Additionally, we discarded noisy force curves and/or curves that presented jumps possibly due to cantilever and plasma membrane adhesion, slippage, or very weakly adhered and moving cells. T cell surface tension (*T*; pN/μm) was computed by fitting each recorded force-distance curve with the surface tension formulae described in (Cartagena-Rivera et al., 2016; Logue et al., 2015) that defines the force balance relating the applied cantilever force with the pressure excess inside the rounded cells and the corresponding surface tension; $T = \frac{kc}{\pi}\left(\frac{1}{\left(\frac{z}{d}\right)-1}\right)$, where *T* is the cellular surface tension, k_c is the AFM cantilever spring constant, *Z* is the Z-piezo extension, and *d* is the cantilever mean deflection. Additionally, the T cells intracellular hydrostatic pressure (*P*; Pa) was calculated by using Laplace's law for spheres; $P = \frac{2T}{R}$, where *P* is the intracellular hydrostatic pressure and *R* is the initial radius of the T cell. AFM analysis was performed by Dr. Alexander X. Cartagena-Rivera.

2.14 Super-Resolution Imaging of human T cells on nanotextured surface and in 3D matrices

Super-Resolution Stimulated Emission Detection (STED) microscopy was performed using a commercial Leica SP8 STED 3× system (Leica Microsystems, Mannheim, Germany), equipped with a white light laser with continuous spectral output between the wavelengths of 470 nm to 670 nm, and a 592 nm, 660 nm and a pulsed 775 nm STED depletion lasers, to obtain time-gated STED images on 3 hybrid detectors. Given the

complexity and varying depth of the sample, we have used the STED WHITE Glycerin objective lens (HC PL APO 93✕/1.30 GLYC motCORR) (Leica Microsystems) which is advantageous for depth imaging due to the motorized correction collar allowing precise and swift adjustment of optical lenses to specimen inhomogeneity. Labeled samples placed in 35 mm culture dishes with number 1.5 cover glass bottom (MatTek Corporation, Ashland, MA) containing 250 µl glycerol (90%) in PBS were imaged in sequentially as follows: first sequence STED for SiR-actin (via 647 nm excitation and 660-730 nm emission range) on gated (0.7- 6.5 ns time gating) hybrid detector using 775 nm (25% power) as STED depletion laser for best lateral resolution; Second and third sequences were confocal settings for Hoechst and Alexa488 (labeling nucleus and surface of the gel) respectively, via two sequential excitations (405 nm, and 488 nm) and two emission ranges (410-465 nm, and 495-555 nm) respectively, on gated (0.3-6.5 ns) hybrid detectors. Imaging was performed with a scan speed of 600 lines per second, scanning bidirectionally, a pixel size of 30-35 nm (1024✕1024 pixels), and 6-line averages, pinhole of 0.7 Airy units and Z-stacks were collected at 0.140 µm-depth intervals throughout the depth of the sample. We deconvoluted images using Huygens Professional software version 18.10.0 (SVI, Hilversum, NL) with the classical maximum likelihood estimation algorithm. We then inspected and reconstructed 3D data using Clear Volume plugin (FIJI). Still frames were saved and montaged using Adobe Photoshop CC.

The instant structured illumination microscopy (iSIM) was performed using an Olympus IX-81 microscope (Olympus Corp., Tokyo, Japan) equipped with an Olympus UPLAPO-HR 100x/1.5 NA objective, two Flash-4 scientific CMOS cameras (Hamamatsu Corp. Tokyo, Japan), an iSIM scan head (VisiTech Intl., Sunderland, UK), and a Nano-Drive piezo Z stage (Mad City Labs, Madison, WI). The iSIM scan head included the VT-Ingwaz optical de-striping unit (VisiTech Intl., Sunderland, UK). Image acquisition and system control was through MetaMorph Premiere software (Molecular Devices, LLC, San Jose, CA). Images were deconvolved using the specific for iSIM commercial plugin from Microvolution (Cupertino, CA) in FIJI. Imaging was performed by Dr. Alexander X. Cartagena-Rivera.

2.15 Statistical analysis

Multiple groups were compared by ANOVA, followed by the Tukey post hoc analysis. Pairwise comparisons were analyzed using a *t* test. Figure legends indicate which statistical test was performed for the data. Statistical analysis was performed using either KaleidaGraph 4.5.3 (Synergy Software) or Prism 7b (GraphPad Software, Inc) software. Unless otherwise mentioned, sample size was pooled from many cells/fields of view (FOVs) over several FOVs. Number of experimental replicates are 3 or more.

Chapter 3. Tumor Slice Culture and Imaging as a Tool to Visualize Live Tumor Dynamics

3.1 Introduction

Tumor slice culture enables the study of the TME comprised of carcinoma, stromal and immune cells and the dense extracellular matrix (ECM) architectures in space and time. Slice culture has been performed on a variety of tissues and solid tumors such as thymus (Dzhagalov et al., 2012), lymph nodes (Asperti-Boursin et al., 2007), lung (Bougherara et al., 2015; Salmon et al., 2012b), liver (Wu et al., 2018), breast (Naipal et al., 2016), brain (Liu et al., 2019), pancreas (Jiang et al., 2017) and among others. Recent studies suggest that slices are responsive to drug treatments (Jiang et al., 2017; Nagaraj et al., 2018; Naipal et al., 2016) making this an ideal platform to study how different drugs can disrupt the TME and providing insights to new approaches in treating cancer .

Non-linear optical imaging platforms such as two-photon imaging and second harmonic generation (SHG) can be employed to visualize the live dynamic processes within the tissue's native environment (Dzhagalov et al., 2012). Two-photon or multiphoton laser scanning microscopy provides several advantages over normal one-photon microscopy. They are: decreased signal scatter which results in greater depth penetration in the tissue, longer wavelength deposit less energy to tissues which decrease phototoxicity which is extremely important for live tissues, high spatial and temporal resolution (similar to confocal microscopy), and SHG allows the visualization of collagen and other biological materials (Benninger and Piston, 2013; Perry et al., 2012; Provenzano et al., 2009). Several studies have shown the benefits of using this tool, in cancer research, for in vivo flow cytometry (He et al., 2007), imaging of circulating tumor cells (Kuo et al., 2019), metastasis (Tanaka et al., 2014), and immune cell function (e.g. cancer killing) (Cazaux et al., 2019). It is known that in many cancers, early detection and resection of primary tumor will have a high chance of survival and remission. Nonetheless, recurrence of cancer, treatment resistance and/or metastasis complications is usually lethal. Understanding of the mechanisms of how tumor cells escape from their site of origin, colonize and thrive in distant tissues as well as how to target metastasis is critical. Thus, combining this powerful imaging tool with live tumor slices will allow the visualization of dynamics in tumors.

3.2 Tumor slice culture and imaging

Live tumor slices can be obtained from genetically engineered *KPC* and *KPCT* mice and cultured for a few days in organotypic inserts (**Fig. 2A**), while preserving native tissue architecture (**Fig. 2B**). Also, mCD8+ T cells, isolated from the spleen of tumor bearing *KPC*/*KPCT* mice, can be labeled and plated onto the slices where they readily attach and migrate in the native 3D TME of PDA tumor slice. Imaging, using multiphoton microscopy and SHG, was employed to visualize cells (carcinoma and CD8+ T cells) and collagen architecture (**Fig. 2B, C**). As previously mentioned, this type of imaging provides superior benefits than conventional confocal microscopy as it is possible to image deeper in the tissue while reducing photobleaching and phototoxicity. Furthermore, we can use Trackmate to track the migration of plated mCD8+ T cells on tumor slices (**Fig. 2D**). Although not performed in T cells in this study, there is evidence that you can live stain tissues to image resident CD8+ T cells in several tumor slices (e.g. pancreas (Jiang et al., 2017), lung and ovaries (Bougherara et al., 2015)). This may suggest that other cell types may be stained and studied as to how different cell types migrate within tumors. Tumor slice culture and imaging serves as a promising tool to study the 3D dynamic interaction and relationship between cell populations and the ECM environment and potentially elucidating the mechanisms of disease progression in order to develop novel therapeutic interventions.

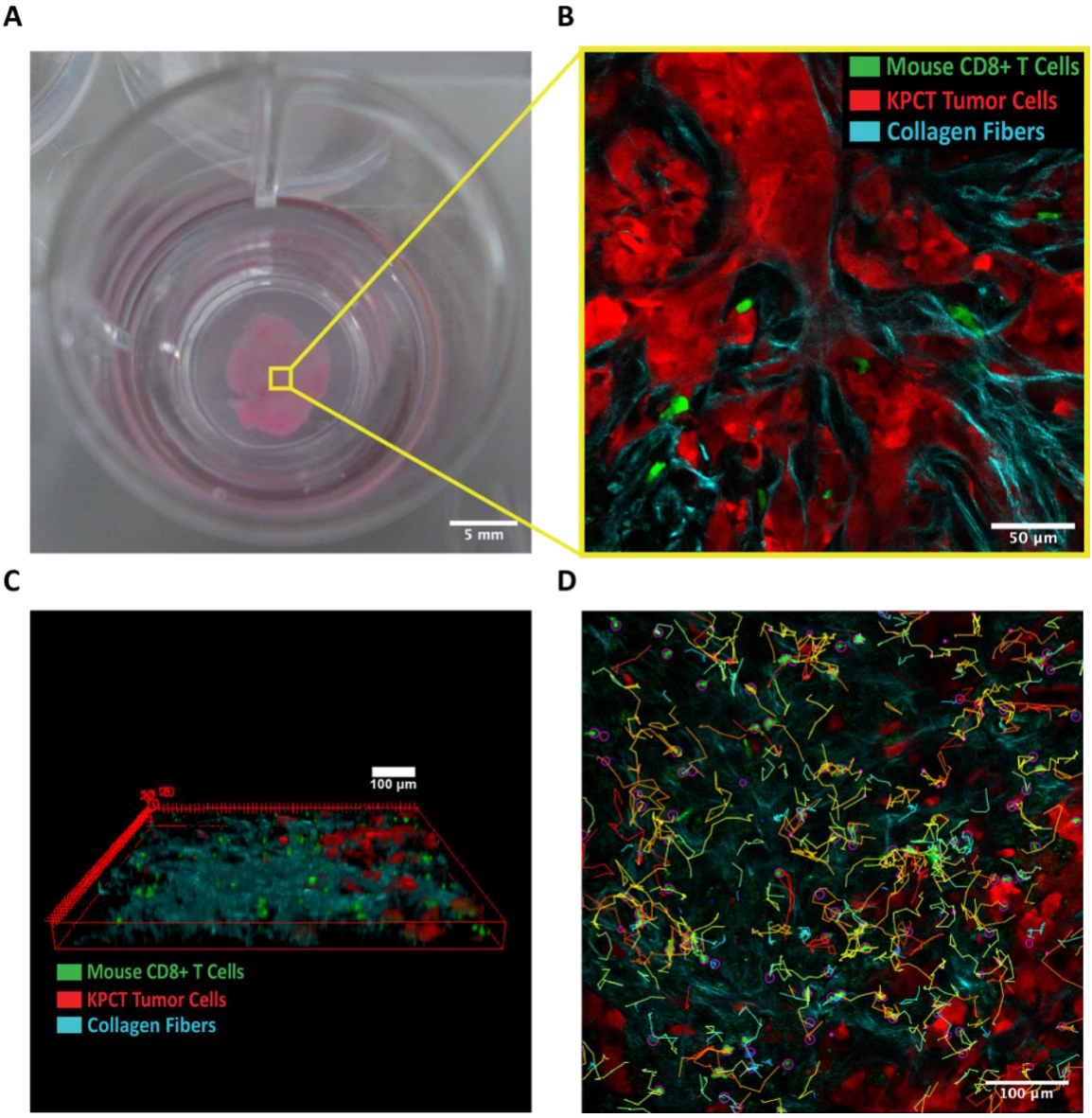

Figure 2: KPCT tumor slice culture, imaging and tracking. (**A**) *KPCT* tumor slice culture in 24-well plate organotypic culture insert. Scale bar = 5 mm. (**B**) Representative single live imaging from a slice within a z-stack of *KPCT* tumor cells (red), celltracker green stained mCD8+ T cells (green) and collagen fibers (cyan) using two photon microscopy and SHG. Scale bar = 50 µm. (**C**) 3D rendering of a 75 µm z-stack of plated mCD8+ T cells (green) migrating in *KPCT* tumor slices (red) surrounded by collagen (cyan). Scale bar = 100 µm. (**D**) Representative trackmate tracks from z-stack of (C). Scale bar = 100 µm.

3.3 T cell migration in metastatic sites

Metastasis is a multifaceted and dynamic process involving tumor cells to locally invade and migrate into the surrounding stroma, followed by entry into the vasculature (intravasation), transit and survival within vasculature, exit from the vasculature (extravasation), and growth in a distant tissue (Provenzano et al., 2009; Sahai, 2007). PDA is associated with a high metastatic rate with the liver being the preferential site of metastasis (Houg and Bijlsma, 2018) while other common sites include the lungs and peritoneum but has been virtually seen in many organs (Yachida and Iacobuzio-Donahue, 2009). Using fluorescent reporter mouse model, *KPCT*, offers superior benefit when studying metastasis as tdTomato^{+} carcinoma cells can be visualized in secondary/metastatic sites. Not only can you visualize this through fluorescence but also with the naked eye during harvesting. The normal pancreas in *KPC* mice has a whitish appearance while *KPCT* pancreas show a distinct physical reddish color (**Fig. 3A**) that, when disease is very advanced, metastasis, even if small, can be easily seen during harvesting in various organs, such as the liver (**Fig. 3B**). This raised the interest of live imaging PDA metastasis and mCD8^{+} T cell migration in metastatic sites such as the liver from *KPCT* mice with advanced disease. TdTomato^{+} PDA metastasis can be seen present in the liver as well as a single carcinoma cell migrating along collagen fibers (**Fig. 3C and movie 1**). Plated mCD8^{+} T cells can be seen moving readily on the liver slice and, interestingly, they can also migrate along collagen fibers (**Fig. 3D and movie 2**), via contact guidance, as has been previously reported (Pruitt et al., 2019). This shows that, not only is the tissue viable, the *KPCT* mouse model provides superior benefits, compared to the *KPC* mouse model, when it comes to visualizing PDA, metastasis, and how cytotoxic T lymphocytes interact with diseased tissues.

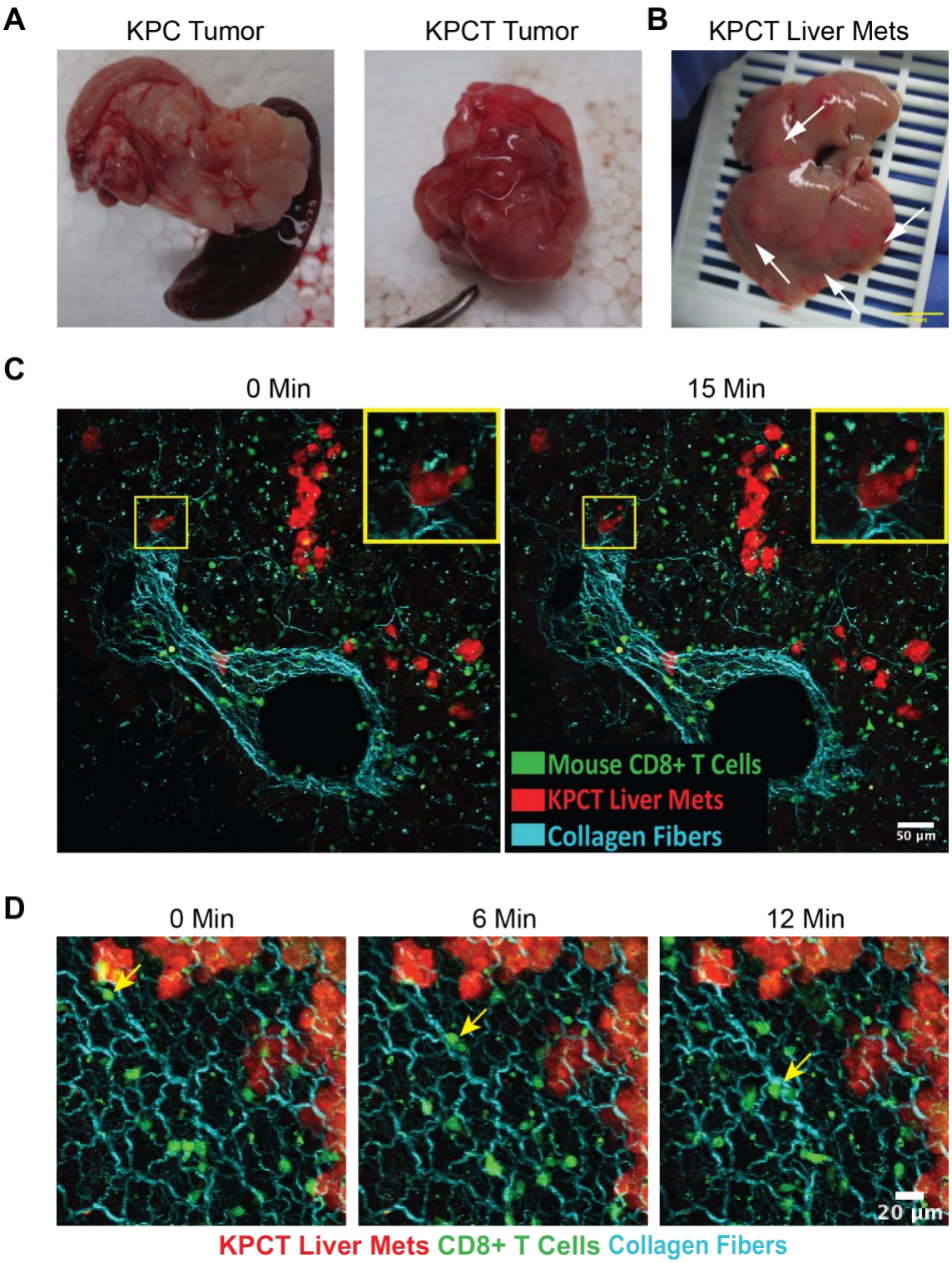

Figure 3: Live imaging of mCD8+ T cells migrating in liver slices with PDA metastasis. (**A**) Freshly harvested *KPC* and *KPCT* pancreas tumors with distinct physical color. (**B**) Freshly harvested *KPCT* liver with multiple visible metastasis indicated by white arrows. Scale bar = 5mm. (**C**) Live imaging of mCD8+ T

cells migrating in liver slices containing PDA metastasis (Mets) from *KPCT* mouse. *Inset* shows magnified region, enclosed by the yellow box, indicating carcinoma cell migrating along collagen fiber. Images are maximum intensity projections of a 50 µm z-stack. Scale bar = 50 µm. (**D**) Maximum intensity projection of 75µm z-stack of a time-lapse sequence of mCD8+ T cells (green) migrating along aligned collagen (cyan) in live liver slices with mets (red). Images in (D) are magnified from a larger FOVs. Scale bar = 20 µm.

3.4 Conclusion

Here, we propose a method for studying metastasis and T cell migration within tissues using MPLSM and cultured tissue slices from tumor bearing GEMMs of PDA. This method allows us to maintain tissues viable and to monitor the live metastatic process. Also, we can plate T cells on various tissues to study their migratory capabilities and action. Moving on, we propose to characterize carcinoma and T cell migration via modeling. Also, incorporating antigen specific T cells or engineered T cells, that target PDA, will allow us to further characterize their homing and killing effect in different tissues. We could then incorporate several therapeutic strategies that includes chemotherapies, radiotherapies, STTs and immunotherapies to modulate tissue and cell dynamics in hopes of increasing the cytotoxic T cell effect in PDA.

Chapter 4. Modulating Disease Response with STT

4.1 Introduction

Dense ECM deposition (e.g. collagen and HA) in TME of PDA tumors acts as barriers for drug delivery (Jacobetz et al., 2013; Provenzano et al., 2012), immune cell activity and infiltration (Jiang et al., 2016; Kuczek et al., 2019), and promote disease progression (Ray et al., submitted). Also, TACS-3-like aligned collagen patterns lead to increased focal invasion and metastasis (Provenzano et al., 2006, 2008b) and correlate with worse survival in human patients (Conklin et al., 2011; Drifka et al., 2016). Yet, while the recent studies suggest the presence of TACS architectures in PDA (Drifka et al., 2015; Ray et al., 2017b), the prevalence of TACS in PDA, particularly relative to disease stage and early dissemination remains largely unexplored. Thus, we hypothesized that TACS or TACS-like collagen architectures are involved in early dissemination and invasion in PDA.

Studies, focused on targeting the stroma in PDA, have been able to dismantle the dense ECM improving drug delivery and disease outcome (Chauhan et al., 2013; Jacobetz et al., 2013; Provenzano et al., 2012), and improve immune activity (Beatty et al., 2011; Feig et al., 2013; Mitchem et al., 2013) and infiltration (Elahi-Gedwillo et al., 2019; Jiang et al., 2016). No studies, to date, have quantified or correlated ECM architectures to carcinoma invasion frequencies or the change in T cell motility when TME is altered with STTs. Therefore, we hypothesize that STT's will slow down or stop disease advancement while improving immune cells capacity to move through tumors.

4.2 Evolution of collagen organization in PDA

To characterize the deposition and architecture of the dense ECM, in particular fibrillar collagen with disease progression in PDA, we utilized SHG imaging for label-free detection of collagen and MPE for endogenous cellular fluorescence from live and archival tissue samples (**Fig. 4**) enabling quantification of fibrous collagen from the SHG signal (**Supplementary Fig. 1**), while also mapping the localization of the collagen fibers with respect to the tissue architecture. In normal pancreata, little collagen is observed, largely concentrated around the few ducts interspersed in the tissue dominated by acinar cells (**Fig. 1A, E, F, J**). Notably, cancer-adjacent normal (CAN) regions showed elevated levels of

collagen around ductal structures and in between acinar clusters (**Fig. 1B, E, G, J**), suggesting activation of a fibroinflammatory stromal response in regions adjacent to tumor, consistent with the intimate link between fibroblast activity and collagen deposition in PDA development (Kraman et al., 2010; Neesse et al., 2015). This may prime adjacent regions for invasion and contribute epithelial dysfunction in adjacent regions (e.g. acinar dropout, ductal hyperplasia, or acinar to ductal metaplasia (ADM)). Moreover, consistent with the desmoplastic response associated with PDA, robust fibrous collagen was ubiquitous in the periductal areas around PanIN lesions (**Fig. 1C, E, H, J**) and remained pervasive in mature disease (**Fig. 1D, E, I, J**). Overall, these data from human and murine PDA samples demonstrate biased collagen localization around ductal structures in normal pancreata and robustly elevated collagen levels in adjacent normal regions, early PanIN lesions, and PDA.

Since elevated collagen levels in breast carcinomas are organized into specific architectures like TACS-3, which guide local invasion (Provenzano et al., 2006, 2008a, 2008b), we hypothesized that such architectures may also be prevalent in PDA and play a key role in local invasion. This prompted us to characterize the periductal collagen organization in histologically early disease. Generally, collagen deposition in the periductal space rendered the majority of the ducts as TACS-2+, albeit with collagen less tightly bound around ductal structures than TACS-2 architectures observed in mammary carcinomas (Provenzano et al., 2006), while TACS-3 was observed more locally, often associated with invaginations and regions of irregular ductal boundaries (**Fig. 1K-O**). Quantitative analysis of fiber orientations using a Curvelet Transform of the SHG signal in human PDA demonstrates TACS-2 (i.e. parallel collagen distributed around ~0° relative to the epithelial boundary) or TACS-3 (i.e. perpendicular collagen distributed around ~90° to the boundary)-like periductal collagen organization (**Fig. 1K, L**). Notably, in human samples with Stage-I to Stage-IV disease, the presence of TACS architectures was not limited to a particular disease stage (**Fig. 1M**). However, consistent with invasive breast carcinoma (Conklin et al., 2011; Provenzano et al., 2006), there tends to be a higher prevalence of TACS-3+ ducts in more advanced disease (**Fig. 1M**). Yet, a substantial proportion (~40%) of ductal

structures in Stage-I patients also present with TACS-3 (**Fig. 1M**), suggesting that these conduits for invasion are prevalent very early in PDA.

In agreement with human patient data, live imaging of pancreatic tumor sections from *KPCT* or *KPCG* mice confirmed that collagen organized into TACS-2- and TACS-3-like patterns was indeed a distinct feature of the periductal space in both early (~1.5mo) and in histologically well-differentiated late (~6mo) stage disease (**Fig. 1N**). We note that in poorly and undifferentiated disease that lack clear and intact ductal structures, robust regions of aligned collagen are observed throughout the tumor, where we have previously reported directed migration (Ray et al., 2017b). Consistent with human patient data, the frequency of TACS-3+ ducts were higher in advanced well-differentiated PDA as compared to PanIN lesions (**Fig. 1O**). These observations prompted us to posit that TACS architectures, which are closely linked to invasion and metastasis in breast carcinoma, play an important role in the early and extensive metastasis in PDA. This leads us to pursue avenues of targeting the ECM, with STT, as a means to slow and/or stop disease progression.

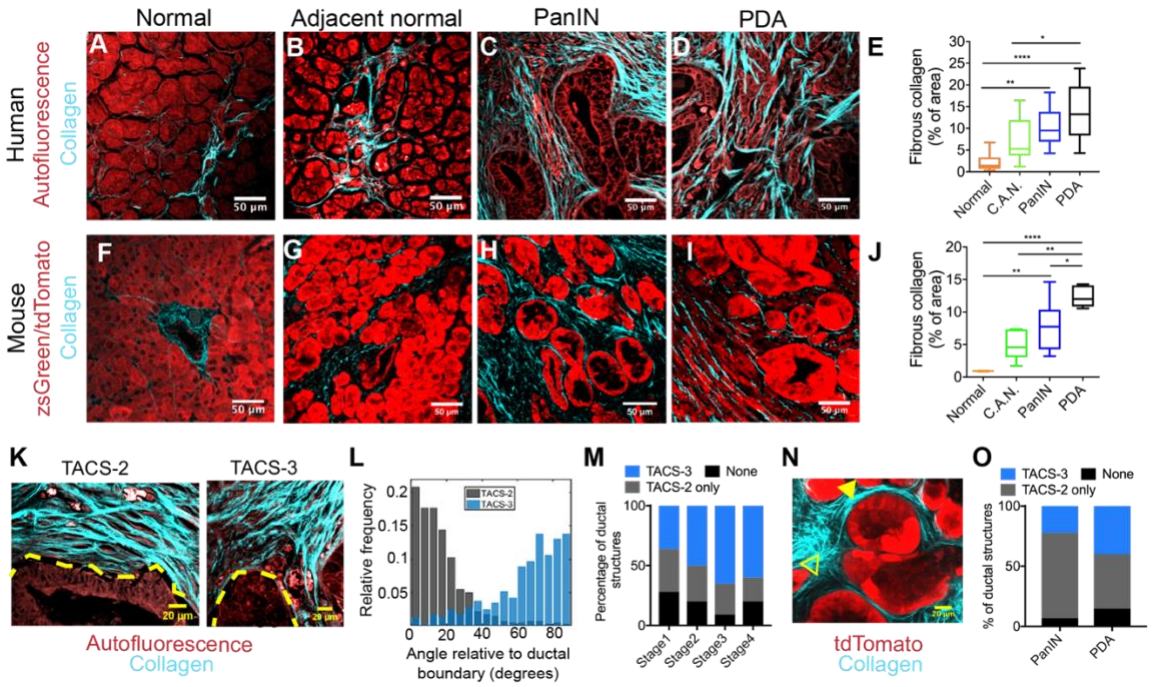

Figure 4: Fibrous collagen architectures in PDA. (**A-D**) Combined multiphoton excitation (MPE) and second harmonic generation (SHG) of human biopsy samples showing tissue architecture by endogenous

fluorescence (autofluorescence) and fibrous collagen by SHG in (A) normal, (B) cancer-adjacent normal (CAN), (C) PanIN and (D) mature PDA. (**E**) Collagen quantification for the data shown in A-D (n = 10-21 fields of view across n ≥ 3 patient biopsies). (**F-I**) Combined MPE/SHG imaging and analysis using *KPCT* or *KPCG* mouse models of PDA for (F) normal, (G) CAN, (H) PanIN and (I) well-differentiated PDA. (**J**) Collagen quantification for the data shown in F-I (n = 5-12 fields of views across n ≥ 3 mice for CAN, PanIN and PDA, n = 3 for normal pancreas). (**K-L**) Representative TACS-2 and TACS-3 positive ducts in human PDA showing parallel and perpendicular alignment of fibrous collagen, with yellow dashed lines indicating ductal boundaries (K), quantified by CT-FIRE (L). (**M**) Frequency of TACS-2 and TACS-3 associated with different stages of human disease showing increased prevalence TACS-3 with more advanced disease. (**N**) Example of collagen architectures in early stage disease (1.5mo) in a *KPCT* mouse (outlined and solid arrowhead point to TACS-3 and TACS-2 respectively). (**O**) Frequency of quantified TACS associated with PanIN lesions and well-differentiated PDA genetically engineered mice. Scale bars = 50 μm (A-D, F-I) and 20 μm (K, N), box-whisker plots show min to max with median and interquartile range for E and J. Significance was determined by one-way ANOVA and the non-parametric Kruskal-Wallis test and Dunn's multiple comparison test * p-value < 0.05, ** p-value < 0.01, **** p-value < 0.0001. Ray et al., submitted.

4.3 STT in PDA to slow down disease progression

It is well established that carcinoma cells follow contact guidance cues in the form of aligned collagen structures (e.g. TACS) (Provenzano et al., 2006), TACS-2 but more effectively TACS-3 (Ray et al., submitted) and that these paths start to develop from early disease. Furthermore, aligned collagen structures are negative prognostic factors for patients with PDA (Drifka et al., 2016). In similar desmoplastic system such as breast carcinoma, pioneer metastatic cells utilize bundles of aligned collagen as highways to escape towards blood vessels (Han et al., 2016). Therefore, we visualized the localization of TACS and extruded cells with respect to $CD31^+$ blood vessels in archival tissue samples. Extruded cells in the stroma were frequently observed in close association with blood vessels in the stroma (**Fig. 5A, B**). In *KPC* mice, extruded single cells were present on aligned collagen fibers leading to open blood vessels (which are less frequent relative to the larger fraction of collapsed vessels in PDA (Elahi-Gedwillo et al., 2019; Provenzano et al., 2012)) in both PanIN lesions as well as mature well-differentiated disease (**Fig. 5A**). Importantly, we confirmed these findings in human tissue samples using pan-cytokeratin to mark cancer cells (**Fig. 5B**). With remarkable consistency, aligned collagen fiber tracks, punctuated with single or streams of multiple carcinoma cells, were observed leading to

CD31+ blood vessels (**Fig. 5B**). It is important to note that while a large percentage (~75%) of blood vessels in mature PDA are collapsed and non-perfused (Olive et al., 2009; Provenzano et al., 2012), those in the early stages of the disease have a much higher likelihood of being open (Elahi-Gedwillo et al., 2019) and thereby provide a more clear passage for these constantly extruding cells to escape and enter the bloodstream. Taken together, these data strongly suggest that the phenomenon of early extrusion and invasion along organized collagen fibers plays a direct role in early and extensive metastasis observed in PDA. We also note that this program is prevalent through all stages of disease, actively and continually promoting disease spread, suggesting that disrupting this process with STT's may be a viable strategy to slow or halt disease progression during therapeutic interventions to combat already established primary and metastatic disease.

Interestingly, TACS have also been found in human chronic pancreatitis (CP) (**Fig. 5C**), a disease which represents a strong risk factor for development of PDA and can be a precursor to malignancy (Becker, 2014; Kong et al., 2014). Further examination in a tissue microarray (**Supplementary Fig. 2**) from 6 patients with human CP revealed an abundance of TACS-2 and TACS-3 in association with ductal structures (**Fig. 5D**) in which every patient sample presented with ducts that were TACS-3+. Moreover, these data suggest that fibroinflammatory diseases that may precede PDA, such as pancreatitis, can result in stromal ECM architectures primed to facilitate disease spread from the earliest onset of disease. This suggests that STT's focusing on resolving the fibroinflammatory reaction, to disrupt ECM architectures that aid in disease spreading, may be beneficial to impede early cancer dissemination in patients with PDA or who will later develop PDA following previous fibroinflammatory disease in the pancreas.

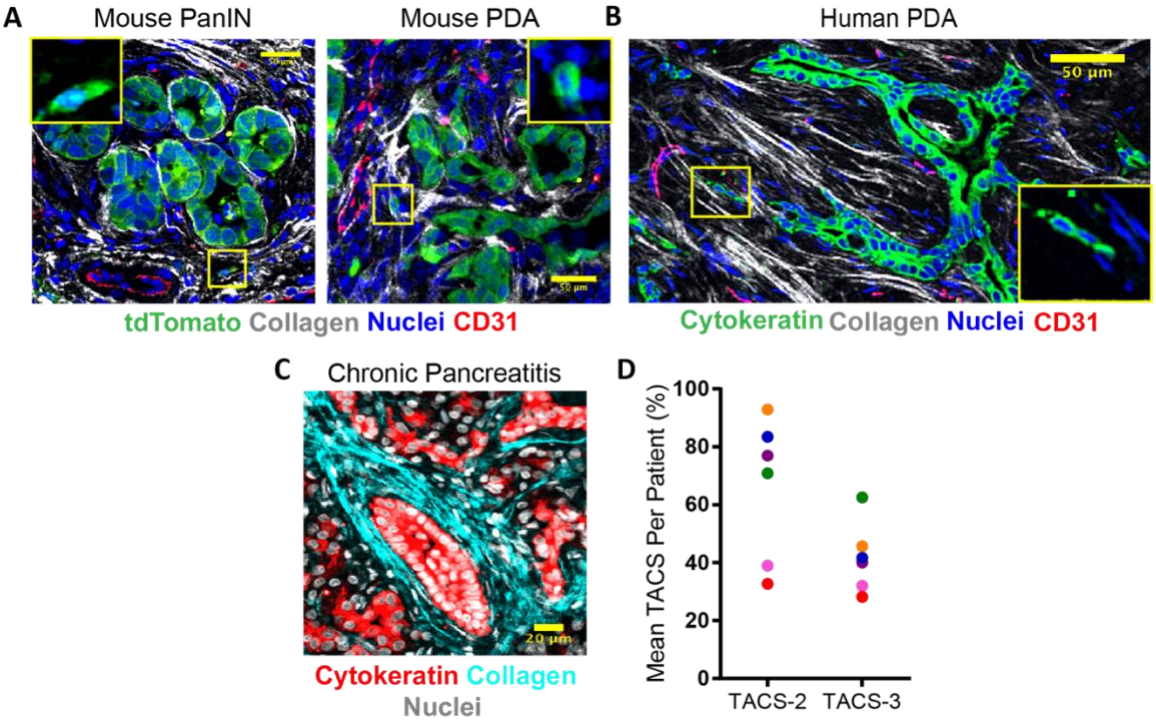

Figure 5: Aligned collagen architectures help guide cell migration. (**A**) Immunofluorescence imaging of *KPCT* tumor sections stained with RFP, CD31 and DRAQ5, demonstrating single extruded cells interacting with aligned periductal collagen in the proximity of blood vessels in mouse PanIN lesions and mature PDA, *inset* shows magnified region enclosed by the yellow box. (**B**) Immunofluorescence imaging of human PDA section stained with Cytokeratin, CD31 and DRAQ5 showing aligned extruded cells following collagen tracks leading to a blood vessel, *inset* shows magnified region enclosed by the yellow box. (**C**) Collagen architecture surrounding ducts in human chronic pancreatitis (CP). (**D**) Frequency of TACS-2 and TACS-3 in association with ductal structures in human CP (Analysis is from 8-33 FOVs from two biopsies per patient from 6 patients with human CP. Note, every patient sample presented with ducts that were TACS-3+) (**E**) Maximum intensity projection of 75µm z-stack of a time-lapse sequence of mCD8+ T cells (green) migrating along aligned collagen (grey) in live liver slices with metastasis (red). Scale bars = 50 µm (A, B) and 20 µm (C, E). Figure panels extracted from Ray et al., submitted.

STTs have the capabilities of having multiple beneficial actions in remodeling the stroma and reducing pathways to metastasis. Previous work using the *KPC* model demonstrated that FAKi leads to a decrease in fibrosis in PDA, with concomitant reduction in the number of invasive PDA cells observed in the periductal space (Jiang et al., 2016). We therefore analyzed PDA FFPE sections from Vehicle vs. FAKi treated groups, obtained from the

FAKi study (Jiang et al., 2016), to analyze cell extrusion and invasion in the context of collagen fiber organization and to study its potential use as a STT. Consistent with the previous findings, FAKi hampers disease progression by slowing down disease advancement represented by a more organized ductal morphology (**Fig. 6A and B**). Furthermore, FAKi also reduces fibrosis in both early and end stage *KPC* mice (**Fig. 6C**) and breaks down the presence of TACS architecture (**Fig. 6D**). As expected, the number of disseminating PDA cells was significantly decreased when subjected to FAKi treatment (**Fig. 6E**). Indeed, TACS-3 is the preferential route that PDA cells use to escape ductal structures as higher extrusion events correlated with TACS-3 (**Fig. 6F**), this goes in line with what has been reported in breast cancer (Provenzano et al. 2006, 2008b). Interestingly, there was a significant decrease in extrusion events in correlation to TACS upon FAKi treatment (**Fig. 6F**), thus reducing the metastatic capability of carcinoma cells in PDA in relation with TACS overall to other organs (**Fig. 6E-G**). This reduction in fibrosis can be likely attributed to an attenuation of FAK-dependent mechanotransduction in myofibroblasts that regulates the fibroinflammatory response in PDA (Lachowski et al., 2017). In addition to this, it has been reported that FAK inhibition renders PDA responsive to chemotherapy and immunotherapy; increasing survival and the presence of immune cells, specifically $CD8^+$ T cells (Jiang et al., 2016). This confirms that FAKi can serve as an important STT and that it can increase the efficacy of chemotherapies and immunotherapies that, when in combination with other therapies (STTs, inhibitors, chemotherapies and immunotherapies), may pose a synergistic effect in treating solid tumors such as PDA.

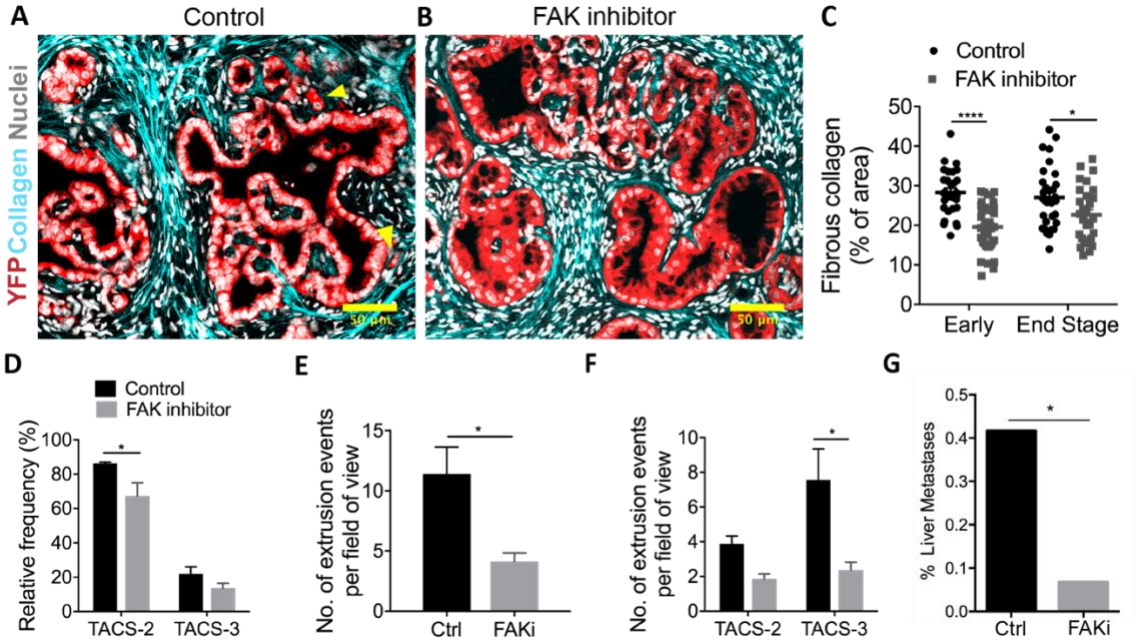

Figure 6: Inhibition of FAK disrupts collagen architectures, extrusion and metastasis in PDA. (**A, B**) Immunofluorescence imaging of stained *KPCY* sections either treated with (**A**) vehicle control or (**B**) FAK inhibitor showing reduction in collagen deposition around ductal structures, smoother ductal boundaries and reduction in cell extrusion, *yellow arrowheads* indicate single cell extrusion events in the control sample. (**C**) Quantification of collagen content in *KPC* mice shows a reduction in deposition of fibrous collagen in both early (1.5 month) and end stage mice, with a (**D**) reduction in TACS-like architectures. (**E**) Number of extrusion events quantified from images related to A-B, D showing reduced extrusion by FAK inhibition. (**F**) Extrusion events for the control and FAK inhibited groups quantified as a function of TACS-2 or TACS-3-related architectures. (**G**) re-plotting of data reported by *Jiang et. al* showing reduction in liver metastases in *KPC* mice treated with FAK inhibitor (Jiang et al., 2016). Scale bars = 50μm. Data represents mean +/- SEM with n >= 3 per group (C, E) and n = 29-36 FOVs per group (D, F). Significance determined using 2-way ANOVA and Sidak's multiple comparison test (C, D, F), by Student's t- test using Hold-Sidak method (E), and Fisher's exact test (g) * *p*-value < 0.05, **** *p*-value < 0.0001. Ray et al., submitted.

4.4 STT can be used to improve T cell motility in PDA

Here, time-lapse imaging, using multiphoton microscopy and SHG, was employed to capture the physical and dynamical changes that STT, with collagenase or hyaluronidase, have on *KPC*/*KPCT* tumor slices. It can be observed that collagen can be completely ablated from the FOV when treating the tumor slice with collagenase (**Fig. 7A**). HA

ablation cannot be seen since no fluorophore was used to detect it (**Fig. 7A**) but, for both STT treatments, there were physical changes that occurred. When collagen is ablated, there is an expansion of the tissue (**movie 3**) and when HA is ablated, there is shrinkage of the tissue within the FOV (**movie 4**). This effect can be correlated to the changes in IFP within the tissue. In which breaking collagen allows the HA pressure to decrease due to the tissue not having the physical enclosure collagen provided. Similarly, breaking down HA is captured by the tissue contracting, shrinking or swelling reduction which is known to directly lower IFP (Provenzano et al., 2012).

Furthermore, mCD8+ T cells, isolated from the spleen of tumor bearing *KPC*/*KPCT* mice, were plated onto *KPC*/*KPCT* tumor slices, live imaged and tracked (e.g. **Fig. 2D**) to quantify their motility (**Fig. 7B and movie 5**). *KPC*/*KPCT* tumor slices were subjected to STT with collagenase or hyaluronidase and live imaged to study the changes in mCD8+ T cell motility. There is a statistically significant shift in bulk mCD8+ T cell motility on tissues subjected to STT (**Fig. 7C**). This represents, on average, a 10% and 25% increase in mCD8+ T cell motility when subjected to collagenase and hyaluronidase, respectively (**Fig. 7D**). This illustrates that breaking down these barriers allows more efficient sampling of the TME within PDA. This results follows the trend found on human lung (Salmon et al., 2012b) and ovarian (Bougherara et al., 2015) tumors in which T cells localized closer to tumor region with increased motility when there is reduced amount ECM.

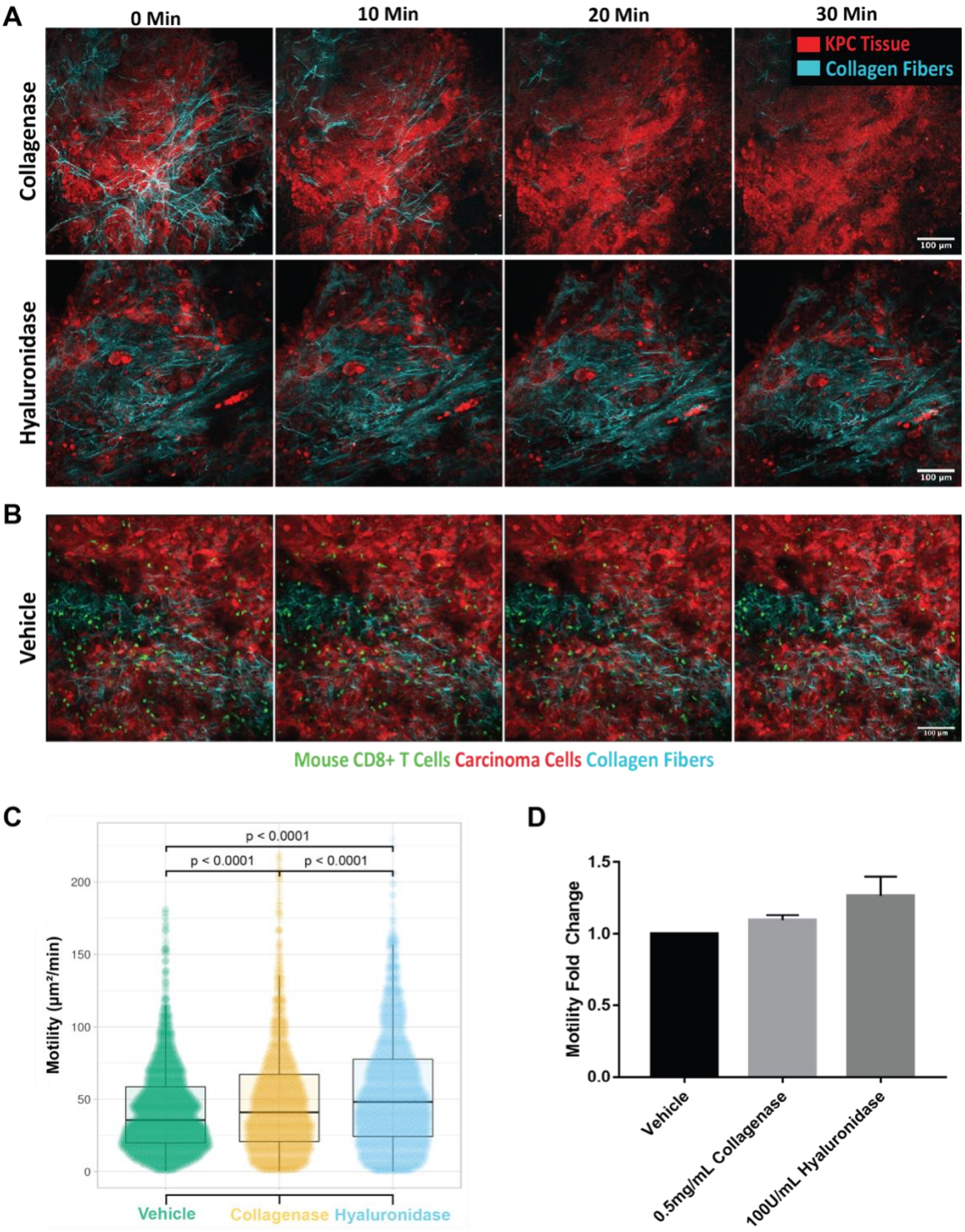

Figure 7: STT re-engineers the stroma enhancing the migratory capabilities of CD8+ T cells. (**A**) Live imaging of *KPC* tumor slices with STT: vehicle (t=0min), 0.5mg/mL collagenase or 100U/mL hyaluronidase for 30 min. Images are maximum intensity projections of a 75 µm z-stack. (**B**) Live imaging of mCD8+ T

cells migrating on *KPCT* tumor slices using the same time intervals as in (A). Images are maximum intensity projections of a 75 µm z-stack. (**C**) Motility in *KPC*/*KPCT* tumor slices subjected to STT. Data represents mean +/- SEM and was pooled from many cells from two FOVs across n ≥ 3 experiments. Significance was determined using One-way ANOVA and Tukey's multiple comparison test. (**D**) Normalized motility data with respect to the vehicle condition. Scale bars = 100 µm.

4.5 Conclusion

Our results show that the microenvironment in pancreatitis, disease that may precede PDA, and early PDA disease, can be primed to facilitate disease spread. Our results also support that early treatment with STT can potentially slow and stop disease advancement by altering the microenvironment within the tumor. We show that using STT can break down solid barriers, directly (e.g. collagen and HA) or indirectly (altering stromal cell behavior e.g. with FAKi), potentially increasing immune surveillance and drug delivery while reducing the metastatic potential of solid tumors such as PDA. We propose to use a combination of STT with other therapies (chemotherapies, immunotherapies) in hopes of synergizing their effect in slowing down disease progression while activating the immune system to efficiently sample the tumor volume to promote a positive immune response.

Chapter 5. Enhancing T Cell Migration Through Structurally and Mechanically Complex Tumor Microenvironments

5.1 Introduction

T cell 3D motility is a combination of steric cell-microenvironment interactions (amoeboid motility), driven by cell shape change, and adhesive cell-microenvironment interplay (mesenchymal motility). Although both mesenchymal and amoeboid motility are tightly intertwined (Talkenberger et al., 2017; Tooley et al., 2009; Wolf et al., 2003), amoeboid motility is predominant and a preferred motility mode during motility along sterically interactive surfaces rather than 2D surfaces (Tabdanov and Rodriguez-Merced et al., submitted). Amoeboid blebbing (**Fig. 8A**) dynamics is directly linked to actomyosin contractility (Ruprecht et al., 2015). We have chosen to control T cell contractility by either direct targeting of MTs (Heck et al., 2012; Hui and Upadhyaya, 2017; Liu et al., 1998), or via a direct activation (Flatau et al., 1997; Schmidt et al., 1997), or inhibition (Benink and Bement, 2005; Burakov et al., 2003) of RhoA activity. I.e. nocodazole-induced MT destabilization causes *en masse* GEF-H1 release into the cytoplasm (Heck et al., 2012; Krendel et al., 2002), followed by activation of RhoA-MLC phosphorylation cascade and consequent rise of actomyosin contractility (**Fig. 8B**). In contrast, stabilization of the MT network with Taxol depletes GEF-H1 from cytoplasm, causing drop of downstream RhoA activity, therefore low actomyosin contractility (**Fig. 8B**). Alternatively, a direct RhoA activation/inhibition was performed with G-switch™ treatments and used as a direct positive control. We have shown that altering the external factors, or TME via STT, modulates T cell motility. Now we aim to target internal factors (I.e. MTs) directly in T cells. Specifically to study the changes in mCD8+ and hCD4+ T cell motility, in both 3D collagen-FN matrices and live tumor slices, upon modulating contractility and MT→GEF-H1→RhoA pathway with the goal to control or harness the amoeboid-mesenchymal balance (**Fig. 8B, C**) in T cells to engineer cells capable of sampling tumor volume more readily.

5.2 Controlling T cell migration in 3D environments through the Microtubule-Contractility axis

MT targeting results indicate that, along with the universal shift towards amoeboid phenotype with nocodazole treatment (Tabdanov and Rodriguez-Merced et al., submitted), MT destabilization (+Nocodazole) increases the hCD4+ mechanical rigidity, or stiffening, as a function of actomyosin contractility, conclusively demonstrated by atomic force microscopy (AFM) global cell rigidity probing (**Fig. 8D**). Conversely, microtubular stabilization (+Taxol) induces substantial shift from invasive amoeboid phenotype toward the mesenchymal T cell spreading (Tabdanov and Rodriguez-Merced et al., submitted). Interestingly, Taxol also induces passive T cell rigidification and increased hydrostatic pressure, however, this stiffening was more independent of actomyosin contractility, as addition of Blebbistatin did not soften cells or reduce pressure as profoundly as in control or Nocodazole treatment conditions (**Fig. 8D**). Thus, we attributed Taxol-induced rigidification to the mechanical solidification of Taxol-stabilized microtubules (Cheng and Donhauser, 2013; Elie-Caille et al., 2007; Sun et al., 2009), strongly in line with the recently identified contribution of scaffolding microtubules into the overall active cell mechanics (Tabdanov et al., 2018). Direct targeting of RhoA activity with G-switch™ (RhoA activator vs. inhibitor) displays similar trends previously established for indirect RhoA targeting via MT destabilization (+Nocodazole⟶RhoA activation) or MT stabilization (+Taxol⟶RhoA inhibition). I.e. hCD4+ T cell mechanical rigidity (actomyosin contractility) increases or decreases upon RhoA activation or inhibition, respectively (**Fig. 8D**).

Next, we cross-correlated both hCD4+ and mCD8+ T cells contractility to their 3D migration (I.e. speed and motility) within 3D collagen-FN matrices (**Fig. 8A and movie 6**) using the persistent random walk model. In both hCD4+ and mCD8+ T cells, MT destabilization with Nocodazole significantly increases speed by ~50-100% and overall motility (**Fig. 8E**) ~2-4 fold suggesting that MT destabilizing agents have the potential to enhance T cell migration in tumor-like architectures. The opposite effect was observed when stabilizing MT with Taxol (**Fig. 8E**). Likewise, similar strategies may be employed to enhance Rho activation as an increase in migration was observed in hCD4+ T cells

following Rho activation which is consistent with increases following MT destabilization, while inhibition of Rho again decreases speed and overall motility (**Fig. 8E**). Thus, manipulating the microtubule-contractility axis has the potential to significantly enhance T cell migration through ECM architectures found in tumors and therefore may provide a strategy to enhance migration of therapeutic T cells (e.g. CAR-T cells or other engineered T cells) or native T cells during immunotherapy (e.g. Immune checkpoint blockade).

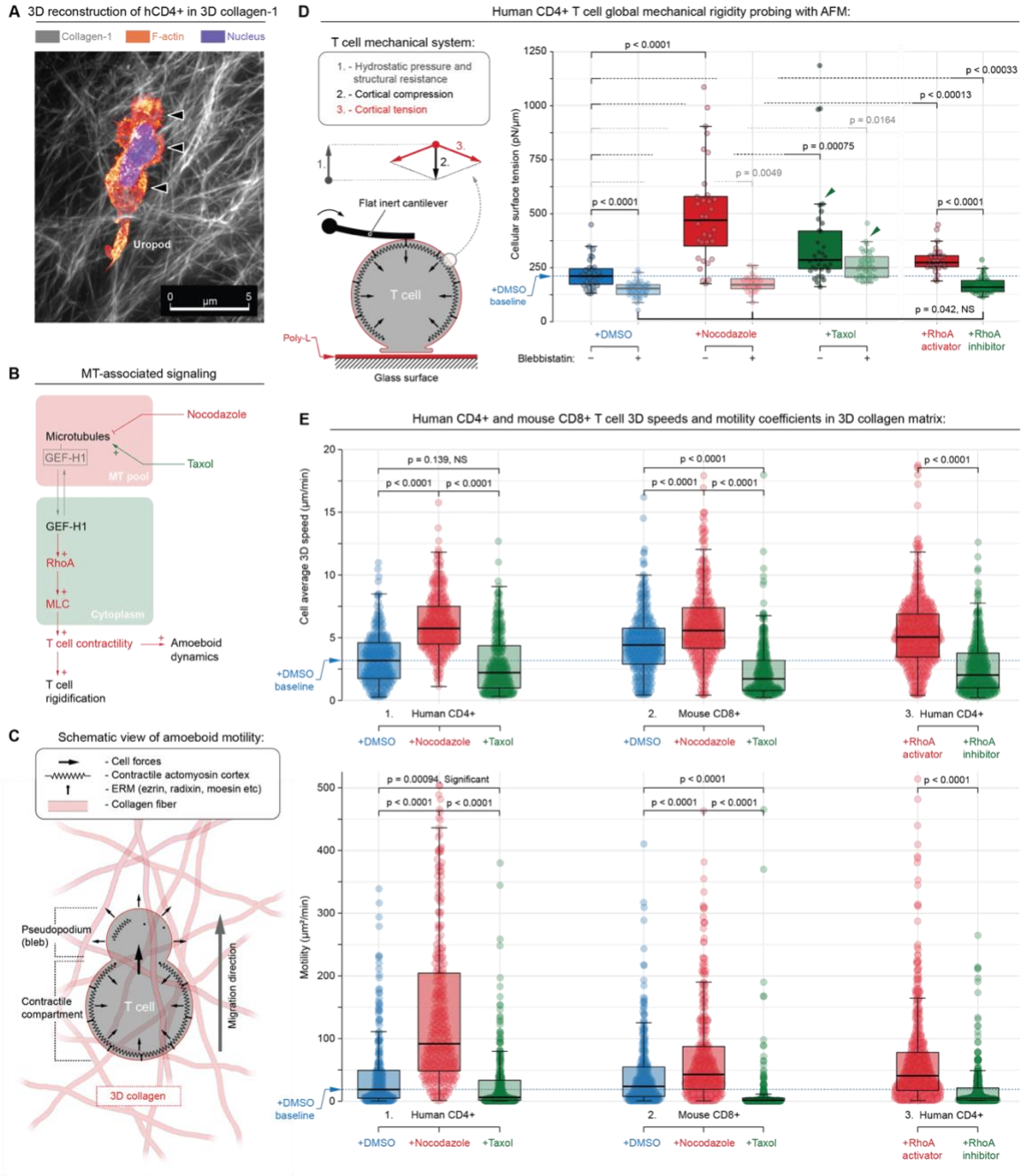

Figure 8: The microtubule-contractility axis regulates T cell mechanics and migration in 3D environments. (**A**) - 3D STED micrograph of hCD4+ migrating through collagen-FN matrix. *Arrowheads* - distinct blebb-like amoeboid compartments. Scale bar = 5 µm. Imaging was performed by Dr. Alexander X. Cartagena-Rivera. (**B**) - MT-associated signaling integrates amoeboid motility, contractility and MT stability via GEF-H1 "cytoplasm⇄MT" reversible transitioning. (**C**) - T cell amoeboid motility is linked to actomyosin contractility: cortex tension-induced hydrostatic pressure forces plasma membrane off-cortex

peeling (blebbing), resulting in pseudopodia formation. Continuous pseudopodial formation facilitates cell's steric interaction with 3D microenvironment, i.e. persistent amoeboid motility. (**D**) *Left* - T cell global compression with flat cantilever measures the overall cortical tension, counterbalanced with cytoplasm hydrostatic pressure (Tabdanov and Rodriguez-Merced et al., submitted) and intracellular structural resistance (microtubules, nucleus etc). *Right* - Atomic force microscopy (AFM) measurement of the global T cell surface tension, i.e. cortical contractility. The control group and each of the two MT-targeting treatments (i.e., +DMSO, +Nocodazole and +Taxol, *solid colors*) are paired with blebbistatin co-treatment (*pale semi-transparent colors*) to verify the key role of actomyosin contractility in change of cell rigidity during MT-targeting. Alternatively, direct RhoA activation/inhibition is compared to MT-perturbation results. Both MT disassembly (+Nocodazole) and direct RhoA activation (+RhoA activator) induce $CD4^+$ cells mechanical rigidification via increased actomyosin tension, as demonstrated by AFM comparison to blebbistatin co-treatment. MT destabilization or direct RhoA activation induced the rise of hydrostatic pressure and a higher resulting cell rigidity. *Note that taxol-induced MTs stabilization increases passive (i.e. actomyosin-independent) T cell rigidity via direct mechanical contribution of stabilized MT scaffold into overall T cell rigidity, as shown by comparison between +Taxol and +Taxol+Blebbistatin treatments (arrowheads).* AFM analysis was performed by Dr. Alexander X. Cartagena-Rivera. (**E**) - 3D speed (*top*) and 3D cell motility (*bottom*) of T cells in 3D collagen-FN matrix: 1 - $hCD4^+$ and 2 - $mCD8^+$ in the presence of vehicle (+DMSO), 10μM Nocodazole (+Nocodazole) or 70nM Taxol (+Taxol); 3 - $hCD4^+$ in the presence of 5μg/mL RhoA activator (+RhoA activator) or 2μg/mL inhibitor (+RhoA inhibitor). Tabdanov and Rodriguez-Merced et al., submitted.

To further test this hypothesis, we imaged the migration of cytotoxic $mCD8^+$ T cells, isolated from *KPC* and *KPCT* mice harboring autochthonous metastatic pancreas cancer, in paired live tumor slices (**Fig. 9A, movies 7 and 8**), with or without MT destabilization. These tissues are composed of the complex heterogeneity of PDA in terms of ECM architecture (e.g. collagen alignment/density) and cell density (e.g. carcinoma and stromal cells) which provides a more robust model to test these principles on. Consistent with our previous findings in 3D environments, microtubule disruption via Nocodazole, specifically in T cells, significantly increased migration of cytotoxic T cells through native tumor environments (**Fig. 9B**), although to a slightly less extent than in 3D collagen-FN matrices which could be attributed to drug delivery, higher complex 3D environment, and uptake competition between plated T cells and tumor slice. These results suggest that destabilizing MTs or perturbing other elements of the MT-contractility axis is indeed a viable strategy to enhance migration of native or therapeutic T cells though structurally complex TMEs.

In stark contrast, T cell exposure to the MT stabilizing agent Taxol results in a significant decrease in both speed and overall motility *in* vitro (**Fig. 8E**) and in live tumor (**Fig. 9B**). This suggests that while Taxane agents can have a beneficial therapeutic impact on carcinoma cells they may also limit the impact of native anti-tumor immunity and that combining T cell-centric immunotherapy approaches (e.g. checkpoint blockade) with taxane agents requires additional scrutiny as these chemotherapies may in fact limit cytotoxic T cell migration into and through tumors.

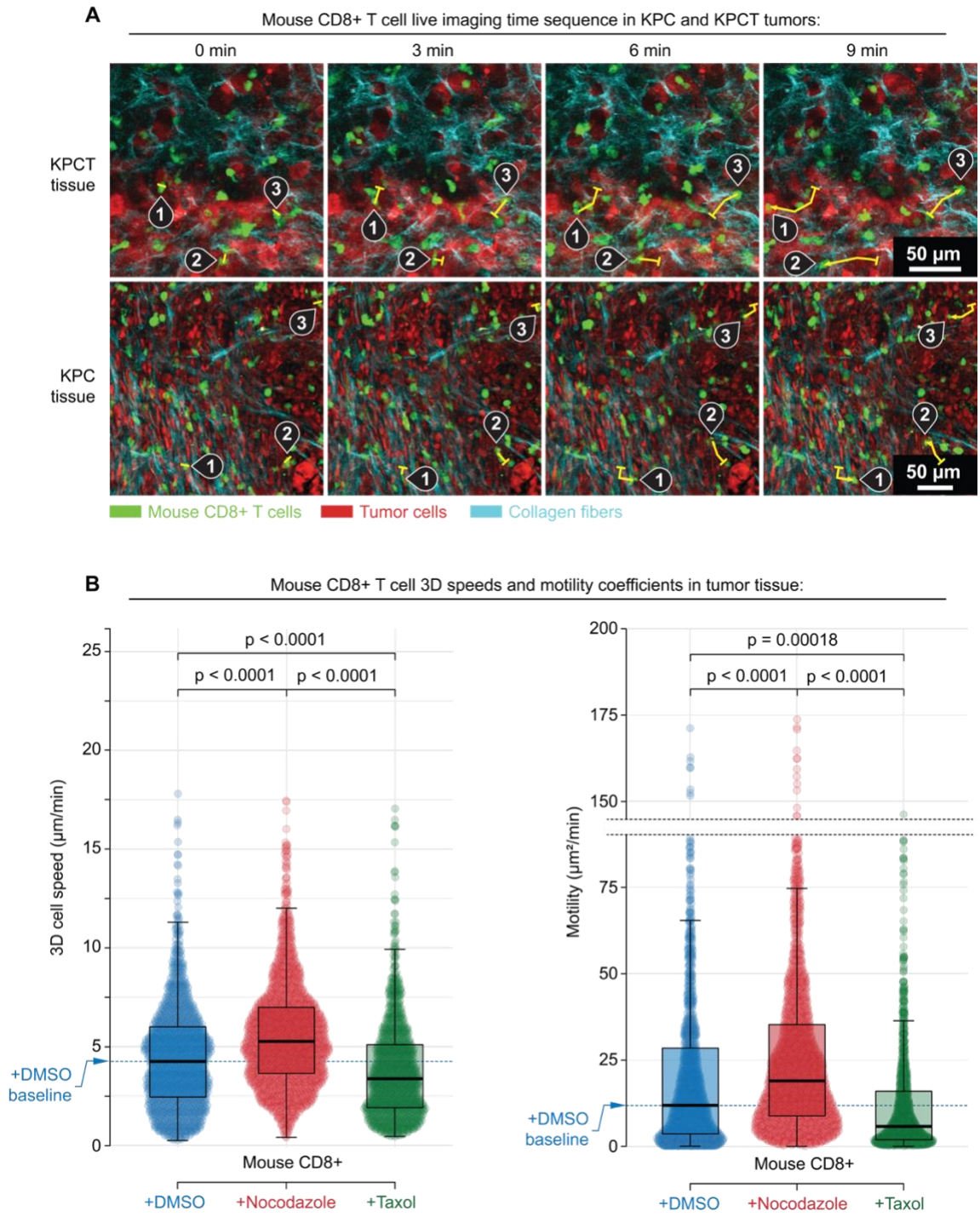

Figure 9: The microtubule-contractility axis regulates Intratumoral migration of cytotoxic T cells. (**A**) Combined multiphoton excitation of fluorescence (MPE) and second harmonic generation (SHG) of primary murine CD8+ cytotoxic T cells (green) in paired live pancreatic tumor from *KPC* mice either expressing tdTomato specifically in carcinoma cells (*KPCT*; *top row*) or with all cells fluorescently labeled (*KPC; bottom row*). Sample migration tracks of individual T cells are highlighted using numerated pins along with

their tracks (yellow curves; *start position - tick, end position - arrowhead*). Images are samples from imaging every 3 minutes for >1hr. Images are MIPs of a 75 μm z-stack. Scale bar = 50 μm. **(B)** Speeds (*left*) and Motility Coefficients (*right*) for cytotoxic T cells migrating within 3D tumor microenvironments under control (+DMSO), MT destabilizing (+Nocodazole), and MT stabilized (+Taxol) treatment conditions, where MT destabilization leads to hypercontractile states and increased migration through stroma dense native pancreatic adenocarcinomas, while treatment with Taxol significantly decreases the ability of T cells to migration through native tumor microenvironments. Tabdanov and Rodriguez-Merced et al., submitted.

5.3 Engineering T cells to improve motility and infiltration capabilities

Our findings indicate that T cell actomyosin contractility and its mechanosensitivity-controlled transmission to the ECM are the main factors controlling T cell transitioning between amoeboid and mesenchymal modes of 3D migration. To further confirm our findings, where GEF-H1/RhoA-regulated T cell contractility improves T cell 3D amoeboid motility and infiltration capabilities, we employed CRISPR technology to engineer hCD4+ T cells that lack GEF-H1 (**Supplementary Fig. 4**). In order to test our hypothesis that Rho activation from Nocodazole-induced MT instability is regulated by GEF-H1, we compared 3D migration of control Cas9 cells and GEF-H1 KO cells in the presence of Nocodazole in 3D matrices (**Fig. 10A**). Consistent with our hypothesis, under MT instability (+Nocodazole), migration is significantly decreased in GEF-H1 KO cells compared to control Cas9 cells, with overall motility cut in half (**Fig. 10B, C**). However, remarkably, in separate experiments we discovered that knockout of GEF-H1 without MT destabilization significantly promotes migration (**Fig. 10D-F**). In 3 human primary activated T cells lines, migration speed through 3D collagen-FN matrices is significantly increased (**Fig. 10E**) while overall motility is significantly increased by more than 50% (**Fig. 10F**), showing that genome engineering to eliminate GEF-H1 can result in engineered T cells that are more capable of migration throughout mechanically and structurally complex environments. Thus, overall these data demonstrate that approaches to alter T cell cytoskeletal-to-contractile machinery and signaling have the potential to significantly enhance T cell movement through complex solid tumor environments. Indeed, genome engineering strategies, or focused pharmacologic targeting, to alter the microtubule-

contractility axis are likely to enhance T cell migration in the therapeutic setting where T cells are often not able to move throughout and sample an entire solid tumor volume.

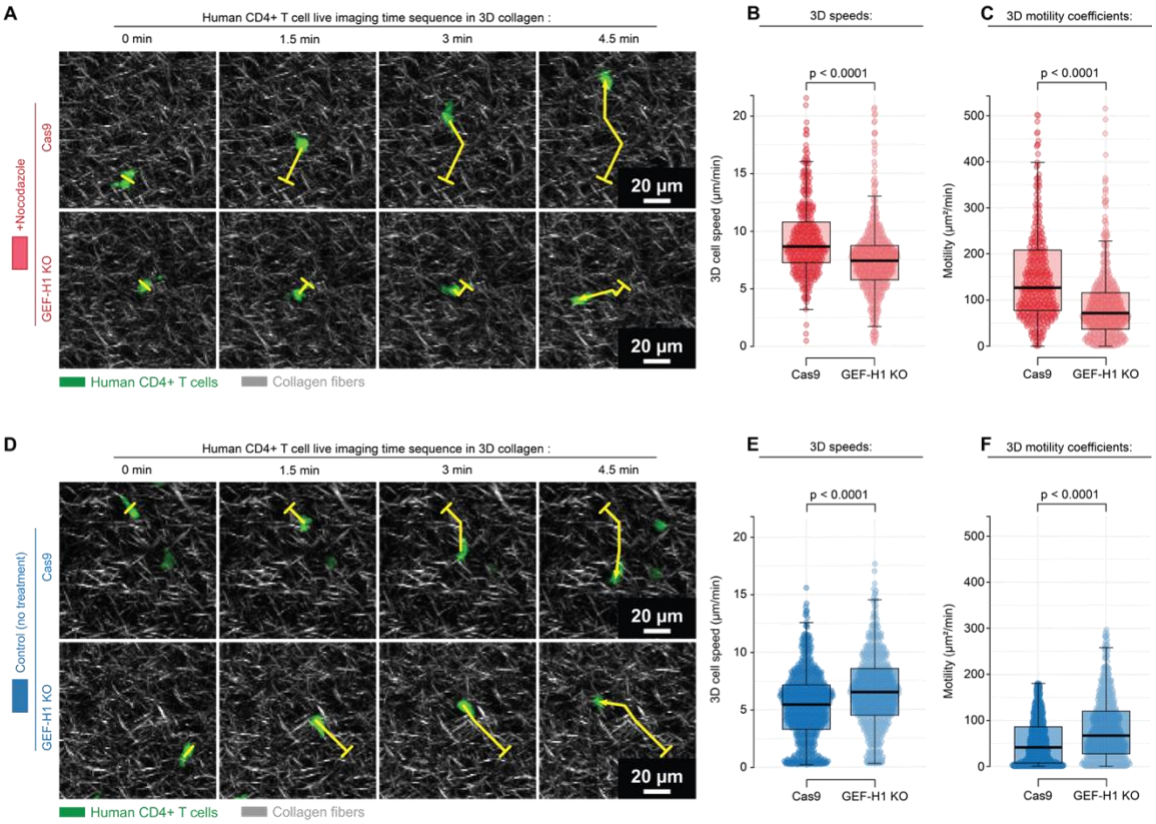

Figure 10: CRISPR GEF-H1 knockout (KO) prevents enhanced migration from microtubule destabilization but enhances migration of untreated T cells. (**A**) Combined multiphoton excitation of fluorescence (MPE) and second harmonic generation (SHG) of primary human T cells (green) migrating through 3D matrices. To test the hypothesis that increased contractility from destabilized microtubules is GEF-H1 dependent, we knocked out GEF-H1 using CRISPR and tested migration over time in the presence of destabilized MTs (+Nocodazole). Samples of migrating T cells are shown and tracks of individual cells are highlighted with their tracks (yellow curves; *start position - tick, end position - arrowhead*). Images are samples from imaging every 1.5 minutes for >1hr. (**B**) Speeds (*left*) and (**C**) Motility Coefficients (*right*) for control (Cas9) and GEF-H1 KO T cells migrating within 3D microenvironments under MT destabilizing conditions (+Nocodazole) showing that loss of GEF-H1 disrupts the contractility-enhanced migration from MT destabilization. Tabdanov and Rodriguez-Merced et al., submitted.

5.4 Conclusion

Here we propose to modulate T cell contractility and MT dynamics in hopes of modulating T cell motility. Our results suggest that chemically increasing or decreasing T cell contractility with Nocodazole or Taxol, respectively, increases and decreases T cell speed and motility, respectively, on hCD4+ and mCD8+ T cells in 3D collagen-FN matrices. We were able to reproduce this trend in a more relevant microenvironment and model, PDA tumor slice from GEMMs, illustrating the capabilities that modulating normal cell dynamics/mechanics have on their motile behavior. Furthermore, in hopes of modulating T cell motility without the use of chemical approaches, we were able to apply CRISPR gene editing technology on hCD4+ T cells to knockout GEF-H1 and modulate the MT→GEF-H1→RhoA pathway. We found that Rho activation Nocodazole-induced MT instability is regulated by GEF-H1 in which knocking out GEF-H1 significantly increases cell speed and motility compared to T cells with native GEF-H1. Furthermore, exposing GEF-H1 KO T cells to MT instability, via Nocodazole treatment, significantly reduced speed and motility compared to native T cells exposed to Nocodazole. Thus, Pharmacological targeting and strategies to apply CRISPR gene editing is likely to enhance T cell migratory capabilities in complex 3D microenvironments. Therefore, these strategies should be used and further explored to enhance migration of native and therapeutic T cells with the aid of other treatments that would synergize their cytotoxic effects on PDA.

Future Work

Here, we were able to produce and maintain live PDA tumor slices and metastatic site slices from GEMMs. Furthermore, we were able to introduce isolated mCD8+ T cells from tumor bearing *KPC*/*KPCT* mice, onto these slices. We propose in the future to include Human slices of PDA and metastatic sites. Although not performed in this study, this method opens that possibility to model and characterize T cells, both plated and resident, or antigen specific T cell decision making in primary and metastatic sites; laying down the foundation to study and target metastasis.

Furthermore, we investigated the dynamic changes in behavior of cells and tissue when modulating external (I.e. STTs) and internal factors (I.e. MTs disruption, cell engineering). Our data suggest that modulating these factors have the potential to increase T cell motility therefore increasing the rate at which these cells sample the tumor volume to have a cytotoxic effect on carcinoma cells. Furthermore, we can incorporate immune checkpoint blockades and perform combination treatments in hopes of synergizing their effect therefore, modulating immunity in PDA.

Limitation of the study

While tumor slices from GEMMs provide several advantages including studying the TME of PDA, stroma targeted therapies and cell migration, it also poses some disadvantages. GEMMs are important preclinical models but still they are not 100% representative of the autochthonous human PDA. Utilizing human PDA slices would reveal native processes in human disease. Also, the imaging frequency, to visualize T cell migration, was in minutes (1.5 min per frame) while T cells move in the seconds range. Also, this limitation only allowed us to image two distinct spots within the sample. To get a smoother imaging and multiple locations within the sample, of the dynamic process of cell migration, resolution can be decreased and/or the resonant scanner can be incorporated, in the multiphoton microscope, to significantly increase sampling frequency. Furthermore, T cell migration analysis was performed on T cells that were plated onto the slices for 1 hour. T cells localization in the tissue was mixed (on top of the slice and within the slice) which could add variability to the data. Another potential study may include imaging resident immune cells within PDA tissue.

Bibliography

Amedei, A., Niccolai, E., Benagiano, M., Della Bella, C., Cianchi, F., Bechi, P., Taddei, A., Bencini, L., Farsi, M., Cappello, P., et al. (2013). Ex vivo analysis of pancreatic cancer-infiltrating T lymphocytes reveals that ENO-specific Tregs accumulate in tumor tissue and inhibit Th1/Th17 effector cell functions. Cancer Immunol. Immunother. *62*, 1249–1260.

Asperti-Boursin, F., Real, E., Bismuth, G., Trautmann, A., and Donnadieu, E. (2007). CCR7 ligands control basal T cell motility within lymph node slices in a phosphoinositide 3–kinase– independent manner. The Journal of Experimental Medicine *204*, 1167–1179.

Beatty, G.L., and Gladney, W.L. (2015). Immune escape mechanisms as a guide for cancer immunotherapy. Clin. Cancer Res. *21*, 687–692.

Beatty, G.L., Chiorean, E.G., Fishman, M.P., Saboury, B., Teitelbaum, U.R., Sun, W., Huhn, R.D., Song, W., Li, D., Sharp, L.L., et al. (2011). CD40 agonists alter tumor stroma and show efficacy against pancreatic carcinoma in mice and humans. Science *331*, 1612–1616.

Becker, A.E. (2014). Pancreatic ductal adenocarcinoma: Risk factors, screening, and early detection. World Journal of Gastroenterology *20*, 11182.

Behrens, D., Walther, W., and Fichtner, I. (2017). Pancreatic cancer models for translational research. Pharmacology & Therapeutics *173*, 146–158.

Benink, H.A., and Bement, W.M. (2005). Concentric zones of active RhoA and Cdc42 around single cell wounds. J. Cell Biol. *168*, 429–439.

Benninger, R.K.P., and Piston, D.W. (2013). Two-Photon Excitation Microscopy for the Study of Living Cells and Tissues. Current Protocols in Cell Biology *59*, 4.11.1–4.11.24.

von Bernstorff, W., Voss, M., Freichel, S., Schmid, A., Vogel, I., Jöhnk, C., Henne-Bruns, D., Kremer, B., and Kalthoff, H. (2001). Systemic and local immunosuppression in pancreatic cancer patients. Clin. Cancer Res. *7*, 925s – 932s.

Bougherara, H., Mansuet-Lupo, A., Alifano, M., Ngô, C., Damotte, D., Le Frère-Belda, M.-A., Donnadieu, E., and Peranzoni, E. (2015). Real-Time Imaging of Resident T Cells in Human Lung and Ovarian Carcinomas Reveals How Different Tumor Microenvironments Control T Lymphocyte Migration. Frontiers in Immunology *6*.

Burakov, A., Nadezhdina, E., Slepchenko, B., and Rodionov, V. (2003). Centrosome positioning in interphase cells. J. Cell Biol. *162*, 963–969.

Burris, H.A., 3rd, Moore, M.J., Andersen, J., Green, M.R., Rothenberg, M.L., Modiano, M.R., Cripps, M.C., Portenoy, R.K., Storniolo, A.M., Tarassoff, P., et al. (1997). Improvements in survival and clinical benefit with gemcitabine as first-line therapy for patients with advanced pancreas cancer: a randomized trial. J. Clin. Oncol. *15*, 2403–2413.

Carlson, M., Watson, A.L., Anderson, L., Largaespada, D.A., and Provenzano, P.P. (2017). Multiphoton fluorescence lifetime imaging of chemotherapy distribution in solid tumors. J. Biomed. Opt. *22*, 1–9.

Carstens, J.L., Correa de Sampaio, P., Yang, D., Barua, S., Wang, H., Rao, A., Allison, J.P., LeBleu, V.S., and Kalluri, R. (2017). Spatial computation of intratumoral T cells correlates with survival of patients with pancreatic cancer. Nat. Commun. *8*, 15095.

Cartagena-Rivera, A.X., Logue, J.S., Waterman, C.M., and Chadwick, R.S. (2016). Actomyosin Cortical Mechanical Properties in Nonadherent Cells Determined by Atomic Force Microscopy. Biophys. J. *110*, 2528–2539.

Cazaux, M., Grandjean, C.L., Lemaître, F., Garcia, Z., Beck, R.J., Milo, I., Postat, J., Beltman, J.B., Cheadle, E.J., and Bousso, P. (2019). Single-cell imaging of CAR T cell activity in vivo reveals extensive functional and anatomical heterogeneity. The Journal of Experimental Medicine *216*, 1038–1049.

Chauhan, V.P., Martin, J.D., Liu, H., Lacorre, D.A., Jain, S.R., Kozin, S.V., Stylianopoulos, T., Mousa, A.S., Han, X., Adstamongkonkul, P., et al. (2013). Angiotensin

inhibition enhances drug delivery and potentiates chemotherapy by decompressing tumour blood vessels. Nat. Commun. *4*, 2516.

Cheng, S., and Donhauser, Z. (2013). GMPCPP and Paclitaxel Effect on Microtubule Stiffness. The FASEB Journal *27*, 1013.3–1013.3.

Clark, C.E., Hingorani, S.R., Mick, R., Combs, C., Tuveson, D.A., and Vonderheide, R.H. (2007). Dynamics of the immune reaction to pancreatic cancer from inception to invasion. Cancer Res. *67*, 9518–9527.

Conklin, M.W., Eickhoff, J.C., Riching, K.M., Pehlke, C.A., Eliceiri, K.W., Provenzano, P.P., Friedl, A., and Keely, P.J. (2011). Aligned collagen is a prognostic signature for survival in human breast carcinoma. Am. J. Pathol. *178*, 1221–1232.

Conroy, T., Desseigne, F., Ychou, M., Bouché, O., Guimbaud, R., Bécouarn, Y., Adenis, A., Raoul, J.-L., Gourgou-Bourgade, S., de la Fouchardière, C., et al. (2011). FOLFIRINOX versus gemcitabine for metastatic pancreatic cancer. N. Engl. J. Med. *364*, 1817–1825.

Cox, T.R., and Erler, J.T. (2011). Remodeling and homeostasis of the extracellular matrix: implications for fibrotic diseases and cancer. Dis. Model. Mech. *4*, 165–178.

Davies, E.J., Dong, M., Gutekunst, M., Närhi, K., van Zoggel, H.J.A.A., Blom, S., Nagaraj, A., Metsalu, T., Oswald, E., Erkens-Schulze, S., et al. (2015). Capturing complex tumour biology in vitro: histological and molecular characterisation of precision cut slices. Sci. Rep. *5*, 17187.

Dickinson, R.B., and Tranquillo, R.T. (1993). Optimal estimation of cell movement indices from the statistical analysis of cell tracking data. AIChE Journal *39*, 1995–2010.

Drifka, C.R., Tod, J., Loeffler, A.G., Liu, Y., Thomas, G.J., Eliceiri, K.W., and Kao, W.J. (2015). Periductal stromal collagen topology of pancreatic ductal adenocarcinoma differs from that of normal and chronic pancreatitis. Mod. Pathol. *28*, 1470–1480.

Drifka, C.R., Loeffler, A.G., Mathewson, K., Keikhosravi, A., Eickhoff, J.C., Liu, Y., Weber, S.M., Kao, W.J., and Eliceiri, K.W. (2016). Highly aligned stromal collagen is a negative prognostic factor following pancreatic ductal adenocarcinoma resection. Oncotarget *7*, 76197–76213.

Dzhagalov, I.L., Melichar, H.J., Ross, J.O., Herzmark, P., and Robey, E.A. (2012). Two-Photon Imaging of the Immune System. Current Protocols in Cytometry.

Elahi-Gedwillo, K.Y., Carlson, M., Zettervall, J., and Provenzano, P.P. (2019). Antifibrotic Therapy Disrupts Stromal Barriers and Modulates the Immune Landscape in Pancreatic Ductal Adenocarcinoma. Cancer Res. *79*, 372–386.

Elie-Caille, C., Severin, F., Helenius, J., Howard, J., Muller, D.J., and Hyman, A.A. (2007). Straight GDP-tubulin protofilaments form in the presence of taxol. Curr. Biol. *17*, 1765–1770.

Emmrich, J., Weber, I., Nausch, M., Sparmann, G., Koch, K., Seyfarth, M., Löhr, M., and Liebe, S. (1998). Immunohistochemical characterization of the pancreatic cellular infiltrate in normal pancreas, chronic pancreatitis and pancreatic carcinoma. Digestion *59*, 192–198.

Feig, C., Gopinathan, A., Neesse, A., Chan, D.S., Cook, N., and Tuveson, D.A. (2012). The Pancreas Cancer Microenvironment. Clinical Cancer Research *18*, 4266–4276.

Feig, C., Jones, J.O., Kraman, M., Wells, R.J.B., Deonarine, A., Chan, D.S., Connell, C.M., Roberts, E.W., Zhao, Q., Caballero, O.L., et al. (2013). Targeting CXCL12 from FAP-expressing carcinoma-associated fibroblasts synergizes with anti-PD-L1 immunotherapy in pancreatic cancer. Proc. Natl. Acad. Sci. U. S. A. *110*, 20212–20217.

Flatau, G., Lemichez, E., Gauthier, M., Chardin, P., Paris, S., Fiorentini, C., and Boquet, P. (1997). Toxin-induced activation of the G protein p21 Rho by deamidation of glutamine. Nature *387*, 729–733.

Franciszkiewicz, K., Boissonnas, A., Boutet, M., Combadière, C., and Mami-Chouaib, F. (2012). Role of chemokines and chemokine receptors in shaping the effector phase of the antitumor immune response. Cancer Res. *72*, 6325–6332.

Friedl, P., and Weigelin, B. (2008). Interstitial leukocyte migration and immune function. Nature Immunology *9*, 960–969.

Fukunaga, A., Miyamoto, M., Cho, Y., Murakami, S., Kawarada, Y., Oshikiri, T., Kato, K., Kurokawa, T., Suzuoki, M., Nakakubo, Y., et al. (2004). CD8+ tumor-infiltrating lymphocytes together with CD4+ tumor-infiltrating lymphocytes and dendritic cells improve the prognosis of patients with pancreatic adenocarcinoma. Pancreas *28*, e26–e31.

Goldstein, D., El-Maraghi, R.H., Hammel, P., Heinemann, V., Kunzmann, V., Sastre, J., Scheithauer, W., Siena, S., Tabernero, J., Teixeira, L., et al. (2015). nab-Paclitaxel plus gemcitabine for metastatic pancreatic cancer: long-term survival from a phase III trial. J. Natl. Cancer Inst. *107*.

Han, W., Chen, S., Yuan, W., Fan, Q., Tian, J., Wang, X., Chen, L., Zhang, X., Wei, W., Liu, R., et al. (2016). Oriented collagen fibers direct tumor cell intravasation. Proc. Natl. Acad. Sci. U. S. A. *113*, 11208–11213.

Harms, B.D., Bassi, G.M., Horwitz, A.R., and Lauffenburger, D.A. (2005). Directional persistence of EGF-induced cell migration is associated with stabilization of lamellipodial protrusions. Biophys. J. *88*, 1479–1488.

Hartmann, N., Giese, N.A., Giese, T., Poschke, I., Offringa, R., Werner, J., and Ryschich, E. (2014). Prevailing role of contact guidance in intrastromal T-cell trapping in human pancreatic cancer. Clin. Cancer Res. *20*, 3422–3433.

He, W., Wang, H., Hartmann, L.C., Cheng, J.-X., and Low, P.S. (2007). In vivo quantitation of rare circulating tumor cells by multiphoton intravital flow cytometry. Proc. Natl. Acad. Sci. U. S. A. *104*, 11760–11765.

Heck, J.N., Ponik, S.M., Garcia-Mendoza, M.G., Pehlke, C.A., Inman, D.R., Eliceiri, K.W., and Keely, P.J. (2012). Microtubules regulate GEF-H1 in response to extracellular matrix stiffness. Mol. Biol. Cell *23*, 2583–2592.

Hingorani, S.R., Wang, L., Multani, A.S., Combs, C., Deramaudt, T.B., Hruban, R.H., Rustgi, A.K., Chang, S., and Tuveson, D.A. (2005). Trp53R172H and KrasG12D cooperate to promote chromosomal instability and widely metastatic pancreatic ductal adenocarcinoma in mice. Cancer Cell *7*, 469–483.

Hingorani, S.R., Bullock, A.J., Seery, T.E., Zheng, L., Sigal, D., Ritch, P.S., Braiteh, F.S., Zalupski, M., Bahary, N., Harris, W.P., et al. (2017). Randomized phase II study of PEGPH20 plus nab-paclitaxel/gemcitabine (PAG) vs AG in patients (Pts) with untreated, metastatic pancreatic ductal adenocarcinoma (mPDA). Journal of Clinical Oncology *35*, 4008–4008.

Houg, D.S., and Bijlsma, M.F. (2018). The hepatic pre-metastatic niche in pancreatic ductal adenocarcinoma. Mol. Cancer *17*, 95.

Hui, K.L., and Upadhyaya, A. (2017). Dynamic microtubules regulate cellular contractility during T-cell activation. Proc. Natl. Acad. Sci. U. S. A. *114*, E4175–E4183.

Hwang, C.-I., Boj, S.F., Clevers, H., and Tuveson, D.A. (2016). Preclinical models of pancreatic ductal adenocarcinoma. The Journal of Pathology *238*, 197–204.

Ino, Y., Yamazaki-Itoh, R., Shimada, K., Iwasaki, M., Kosuge, T., Kanai, Y., and Hiraoka, N. (2013). Immune cell infiltration as an indicator of the immune microenvironment of pancreatic cancer. British Journal of Cancer *108*, 914–923.

Jacobetz, M.A., Chan, D.S., Neesse, A., Bapiro, T.E., Cook, N., Frese, K.K., Feig, C., Nakagawa, T., Caldwell, M.E., Zecchini, H.I., et al. (2013). Hyaluronan impairs vascular function and drug delivery in a mouse model of pancreatic cancer. Gut *62*, 112–120.

Jiang, H., Hegde, S., Knolhoff, B.L., Zhu, Y., Herndon, J.M., Meyer, M.A., Nywening, T.M., Hawkins, W.G., Shapiro, I.M., Weaver, D.T., et al. (2016). Targeting focal adhesion

kinase renders pancreatic cancers responsive to checkpoint immunotherapy. Nat. Med. *22*, 851–860.

Jiang, X., David Seo, Y., Chang, J.H., Coveler, A., Nigjeh, E.N., Pan, S., Jalikis, F., Yeung, R.S., Crispe, I.N., and Pillarisetty, V.G. (2017). Long-lived pancreatic ductal adenocarcinoma slice cultures enable precise study of the immune microenvironment. OncoImmunology e1333210.

Jiang, X., David Seo, Y., Sullivan, K.M., and Pillarisetty, V.G. (2019). Establishment of Slice Cultures as a Tool to Study the Cancer Immune Microenvironment. Methods in Molecular Biology 283–295.

Jones, S., Zhang, X., Parsons, D.W., Lin, J.C.-H., Leary, R.J., Angenendt, P., Mankoo, P., Carter, H., Kamiyama, H., Jimeno, A., et al. (2008). Core signaling pathways in human pancreatic cancers revealed by global genomic analyses. Science *321*, 1801–1806.

Kaur, S., Baine, M.J., Jain, M., Sasson, A.R., and Batra, S.K. (2012). Early diagnosis of pancreatic cancer: challenges and new developments. Biomark. Med. *6*, 597–612.

Kong, X., Sun, T., Kong, F., Du, Y., and Li, Z. (2014). Chronic Pancreatitis and Pancreatic Cancer. Gastrointestinal Tumors *1*, 123–134.

Kraman, M., Bambrough, P.J., Arnold, J.N., Roberts, E.W., Magiera, L., Jones, J.O., Gopinathan, A., Tuveson, D.A., and Fearon, D.T. (2010). Suppression of antitumor immunity by stromal cells expressing fibroblast activation protein-alpha. Science *330*, 827–830.

Krendel, M., Zenke, F.T., and Bokoch, G.M. (2002). Nucleotide exchange factor GEF-H1 mediates cross-talk between microtubules and the actin cytoskeleton. Nat. Cell Biol. *4*, 294–301.

Kuczek, D.E., Larsen, A.M.H., Thorseth, M.-L., Carretta, M., Kalvisa, A., Siersbæk, M.S., Simões, A.M.C., Roslind, A., Engelholm, L.H., Noessner, E., et al. (2019). Collagen density regulates the activity of tumor-infiltrating T cells. J Immunother Cancer *7*, 68.

Kuo, C.W., Chueh, D.-Y., and Chen, P. (2019). Real-time in vivo imaging of subpopulations of circulating tumor cells using antibody conjugated quantum dots. J. Nanobiotechnology *17*, 26.

Lachowski, D., Cortes, E., Pink, D., Chronopoulos, A., Karim, S.A., P Morton, J., and Del Río Hernández, A.E. (2017). Substrate Rigidity Controls Activation and Durotaxis in Pancreatic Stellate Cells. Sci. Rep. *7*, 2506.

Liu, B.P., Chrzanowska-Wodnicka, M., and Burridge, K. (1998). Microtubule depolymerization induces stress fibers, focal adhesions, and DNA synthesis via the GTP-binding protein Rho. Cell Adhes. Commun. *5*, 249–255.

Liu, C.J., Shamsan, G.A., Akkin, T., and Odde, D.J. (2019). Glioma Cell Migration Dynamics in Brain Tissue Assessed by Multimodal Optical Imaging. Biophys. J. *117*, 1179–1188.

Liyanage, U.K., Moore, T.T., Joo, H.-G., Tanaka, Y., Herrmann, V., Doherty, G., Drebin, J.A., Strasberg, S.M., Eberlein, T.J., Goedegebuure, P.S., et al. (2002). Prevalence of Regulatory T Cells Is Increased in Peripheral Blood and Tumor Microenvironment of Patients with Pancreas or Breast Adenocarcinoma. The Journal of Immunology *169*, 2756–2761.

Logue, J.S., Cartagena-Rivera, A.X., Baird, M.A., Davidson, M.W., Chadwick, R.S., and Waterman, C.M. (2015). Erk regulation of actin capping and bundling by Eps8 promotes cortex tension and leader bleb-based migration. Elife *4*, e08314.

Lu, P., Weaver, V.M., and Werb, Z. (2012). The extracellular matrix: A dynamic niche in cancer progression. The Journal of Experimental Medicine *209*, i1–i1.

Martinez-Bosch, N., Vinaixa, J., and Navarro, P. (2018). Immune Evasion in Pancreatic Cancer: From Mechanisms to Therapy. Cancers *10*, 6.

Misra, S., Moro, C.F., Del Chiaro, M., Pouso, S., Sebestyén, A., Löhr, M., Björnstedt, M., and Verbeke, C.S. (2019). Ex vivo organotypic culture system of precision-cut slices of human pancreatic ductal adenocarcinoma. Scientific Reports *9*.

Mitchem, J.B., Brennan, D.J., Knolhoff, B.L., Belt, B.A., Zhu, Y., Sanford, D.E., Belaygorod, L., Carpenter, D., Collins, L., Piwnica-Worms, D., et al. (2013). Targeting tumor-infiltrating macrophages decreases tumor-initiating cells, relieves immunosuppression, and improves chemotherapeutic responses. Cancer Res. *73*, 1128–1141.

Murphy, J.E., Wo, J.Y., Ryan, D.P., Clark, J.W., Jiang, W., Yeap, B.Y., Drapek, L.C., Ly, L., Baglini, C.V., Blaszkowsky, L.S., et al. (2019). Total Neoadjuvant Therapy With FOLFIRINOX in Combination With Losartan Followed by Chemoradiotherapy for Locally Advanced Pancreatic Cancer: A Phase 2 Clinical Trial. JAMA Oncol *5*, 1020–1027.

Nagaraj, A.S., Bao, J., Hemmes, A., Machado, M., Närhi, K., and Verschuren, E.W. (2018). Establishment and Analysis of Tumor Slice Explants As a Prerequisite for Diagnostic Testing. J. Vis. Exp.

Naipal, K.A.T., Verkaik, N.S., Sánchez, H., van Deurzen, C.H.M., den Bakker, M.A., Hoeijmakers, J.H.J., Kanaar, R., Vreeswijk, M.P.G., Jager, A., and van Gent, D.C. (2016). Tumor slice culture system to assess drug response of primary breast cancer. BMC Cancer *16*, 78.

Neesse, A., Algül, H., Tuveson, D.A., and Gress, T.M. (2015). Stromal biology and therapy in pancreatic cancer: a changing paradigm. Gut *64*, 1476–1484.

Ohno, S., Tachibana, M., Fujii, T., Ueda, S., Kubota, H., and Nagasue, N. (2002). Role of stromal collagen in immunomodulation and prognosis of advanced gastric carcinoma. Int. J. Cancer *97*, 770–774.

Olive, K.P., Jacobetz, M.A., Davidson, C.J., Gopinathan, A., McIntyre, D., Honess, D., Madhu, B., Goldgraben, M.A., Caldwell, M.E., Allard, D., et al. (2009). Inhibition of Hedgehog signaling enhances delivery of chemotherapy in a mouse model of pancreatic cancer. Science *324*, 1457–1461.

Othmer, H.G., Dunbar, S.R., and Alt, W. (1987). Models of Dispersal in Biological Systems.

Parslow, A., Cardona, A., and Bryson-Richardson, R.J. (2014). Sample Drift Correction Following 4D Confocal Time-lapse Imaging. Journal of Visualized Experiments.

Peranzoni, E., Rivas-Caicedo, A., Bougherara, H., Salmon, H., and Donnadieu, E. (2013). Positive and negative influence of the matrix architecture on antitumor immune surveillance. Cell. Mol. Life Sci. *70*, 4431–4448.

Perry, S.W., Burke, R.M., and Brown, E.B. (2012). Two-photon and second harmonic microscopy in clinical and translational cancer research. Ann. Biomed. Eng. *40*, 277–291.

Provenzano, P.P., Eliceiri, K.W., Campbell, J.M., Inman, D.R., White, J.G., and Keely, P.J. (2006). Collagen reorganization at the tumor-stromal interface facilitates local invasion. BMC Med. *4*, 38.

Provenzano, P.P., Inman, D.R., Eliceiri, K.W., Knittel, J.G., Yan, L., Rueden, C.T., White, J.G., and Keely, P.J. (2008a). Collagen density promotes mammary tumor initiation and progression. BMC Med. *6*, 11.

Provenzano, P.P., Inman, D.R., Eliceiri, K.W., Trier, S.M., and Keely, P.J. (2008b). Contact guidance mediated three-dimensional cell migration is regulated by Rho/ROCK-dependent matrix reorganization. Biophys. J. *95*, 5374–5384.

Provenzano, P.P., Eliceiri, K.W., and Keely, P.J. (2009). Multiphoton microscopy and fluorescence lifetime imaging microscopy (FLIM) to monitor metastasis and the tumor microenvironment. Clinical & Experimental Metastasis *26*, 357–370.

Provenzano, P.P., Cuevas, C., Chang, A.E., Goel, V.K., Von Hoff, D.D., and Hingorani, S.R. (2012). Enzymatic targeting of the stroma ablates physical barriers to treatment of pancreatic ductal adenocarcinoma. Cancer Cell *21*, 418–429.

Pruitt, H.C., Lewis, D., Ciccaglione, M., Connor, S., Smith, Q., Hickey, J.W., Schneck, J.P., and Gerecht, S. (2019). Collagen fiber structure guides 3D motility of cytotoxic T lymphocytes. Matrix Biol.

Raglow, Z., and Thomas, S.M. (2015). Tumor matrix protein collagen XIα1 in cancer. Cancer Lett. *357*, 448–453.

Ray, A., Callaway, M.K., Rodriguez-Merced, N.J., Crampton, A.L., Carlson, M., Emme, K.B., Ensminger, E.A., Shrope, J.H., Rasmussen, H.R., Jiang, H., Denardo, D.G., Wood, D.K., and Provenzano, P.P. Collagen architecture directs early dissemination in pancreatic ductal adenocarcinoma. Submitted.

Ray, A., Slama, Z.M., Morford, R.K., Madden, S.A., and Provenzano, P.P. (2017a). Enhanced Directional Migration of Cancer Stem Cells in 3D Aligned Collagen Matrices. Biophysical Journal *112*, 1023–1036.

Ray, A., Lee, O., Win, Z., Edwards, R.M., Alford, P.W., Kim, D.-H., and Provenzano, P.P. (2017b). Anisotropic forces from spatially constrained focal adhesions mediate contact guidance directed cell migration. Nat. Commun. *8*, 14923.

Ray, A., Morford, R.K., and Provenzano, P.P. (2018). Cancer Stem Cell Migration in Three-Dimensional Aligned Collagen Matrices. Curr. Protoc. Stem Cell Biol. *46*, e57.

Ruprecht, V., Wieser, S., Callan-Jones, A., Smutny, M., Morita, H., Sako, K., Barone, V., Ritsch-Marte, M., Sixt, M., Voituriez, R., et al. (2015). Cortical contractility triggers a stochastic switch to fast amoeboid cell motility. Cell *160*, 673–685.

Ryschich, E., Nötzel, T., Hinz, U., Autschbach, F., Ferguson, J., Simon, I., Weitz, J., Fröhlich, B., Klar, E., Büchler, M.W., et al. (2005). Control of T-cell-mediated immune response by HLA class I in human pancreatic carcinoma. Clin. Cancer Res. *11*, 498–504.

Sahai, E. (2007). Illuminating the metastatic process. Nature Reviews Cancer *7*, 737–749.

Salmon, H., Franciszkiewicz, K., Damotte, D., Dieu-Nosjean, M.-C., Validire, P., Trautmann, A., Mami-Chouaib, F., and Donnadieu, E. (2012a). Matrix architecture defines the preferential localization and migration of T cells into the stroma of human lung tumors. Journal of Clinical Investigation *122*, 899–910.

Salmon, H., Franciszkiewicz, K., Damotte, D., Dieu-Nosjean, M.-C., Validire, P., Trautmann, A., Mami-Chouaib, F., and Donnadieu, E. (2012b). Matrix architecture defines the preferential localization and migration of T cells into the stroma of human lung tumors. J. Clin. Invest. *122*, 899–910.

Schindelin, J., Arganda-Carreras, I., Frise, E., Kaynig, V., Longair, M., Pietzsch, T., Preibisch, S., Rueden, C., Saalfeld, S., Schmid, B., et al. (2012). Fiji: an open-source platform for biological-image analysis. Nat. Methods *9*, 676–682.

Schmidt, G., Sehr, P., Wilm, M., Selzer, J., Mann, M., and Aktories, K. (1997). Gln 63 of Rho is deamidated by Escherichia coli cytotoxic necrotizing factor-1. Nature *387*, 725–729.

Siegel, R.L., Miller, K.D., and Jemal, A. (2019). Cancer statistics, 2019. CA: A Cancer Journal for Clinicians *69*, 7–34.

Stromnes, I.M., Brockenbrough, J.S., Izeradjene, K., Carlson, M.A., Cuevas, C., Simmons, R.M., Greenberg, P.D., and Hingorani, S.R. (2014). Targeted depletion of an MDSC subset unmasks pancreatic ductal adenocarcinoma to adaptive immunity. Gut *63*, 1769–1781.

Sun, L., Simmerling, C., and Ojima, I. (2009). Recent advances in the study of the bioactive conformation of taxol. ChemMedChem *4*, 719–731.

Tabdanov, E.D., Rodriguez-Merced, N.J., Cartagena-Rivera, A.X., Puram, V., Callaway, M.K., Ensminger, E.A., Pomeroy, E., Yamamoto, K., Lahr, W.S., Webber, B.R., Moriarity, B., Zhovmer, A., and Provenzano, P.P. Enhancing T cell migration through structurally and mechanically complex tumor microenvironments. Submitted.

Tabdanov, E.D., Puram, V., Zhovmer, A., and Provenzano, P.P. (2018). Microtubule-Actomyosin Mechanical Cooperation during Contact Guidance Sensing. Cell Rep. *25*, 328–338.e5.

Talkenberger, K., Cavalcanti-Adam, E.A., Voss-Böhme, A., and Deutsch, A. (2017). Amoeboid-mesenchymal migration plasticity promotes invasion only in complex heterogeneous microenvironments. Sci. Rep. *7*, 9237.

Tan, M.C.B., Goedegebuure, P.S., Belt, B.A., Flaherty, B., Sankpal, N., Gillanders, W.E., Eberlein, T.J., Hsieh, C.-S., and Linehan, D.C. (2009). Disruption of CCR5-Dependent Homing of Regulatory T Cells Inhibits Tumor Growth in a Murine Model of Pancreatic Cancer. The Journal of Immunology *182*, 1746–1755.

Tanaka, K., Toiyama, Y., Okugawa, Y., Okigami, M., Inoue, Y., Uchida, K., Araki, T., Mohri, Y., Mizoguchi, A., and Kusunoki, M. (2014). In vivo optical imaging of cancer metastasis using multiphoton microscopy: a short review. Am. J. Transl. Res. *6*, 179–187.

Tinevez, J.-Y., Perry, N., Schindelin, J., Hoopes, G.M., Reynolds, G.D., Laplantine, E., Bednarek, S.Y., Shorte, S.L., and Eliceiri, K.W. (2017). TrackMate: An open and extensible platform for single-particle tracking. Methods *115*, 80–90.

Tooley, A.J., Gilden, J., Jacobelli, J., Beemiller, P., Trimble, W.S., Kinoshita, M., and Krummel, M.F. (2009). Amoeboid T lymphocytes require the septin cytoskeleton for cortical integrity and persistent motility. Nat. Cell Biol. *11*, 17–26.

Vennin, C., Murphy, K.J., Morton, J.P., Cox, T.R., Pajic, M., and Timpson, P. (2018). Reshaping the Tumor Stroma for Treatment of Pancreatic Cancer. Gastroenterology *154*, 820–838.

Walker, C., Mojares, E., and del Río Hernández, A. (2018). Role of Extracellular Matrix in Development and Cancer Progression. International Journal of Molecular Sciences *19*, 3028.

Wang, M., Zhao, J., Zhang, L., Wei, F., Lian, Y., Wu, Y., Gong, Z., Zhang, S., Zhou, J., Cao, K., et al. (2017). Role of tumor microenvironment in tumorigenesis. J. Cancer *8*, 761–773.

Wolf, K., Müller, R., Borgmann, S., Bröcker, E.-B., and Friedl, P. (2003). Amoeboid shape change and contact guidance: T-lymphocyte crawling through fibrillar collagen is independent of matrix remodeling by MMPs and other proteases. Blood *102*, 3262–3269.

Wu, X., Roberto, J.B., Knupp, A., Kenerson, H.L., Truong, C.D., Yuen, S.Y., Brempelis, K.J., Tuefferd, M., Chen, A., Horton, H., et al. (2018). Precision-cut human liver slice cultures as an immunological platform. J. Immunol. Methods *455*, 71–79.

Yachida, S., and Iacobuzio-Donahue, C.A. (2009). The pathology and genetics of metastatic pancreatic cancer. Arch. Pathol. Lab. Med. *133*, 413–422.

Zhao, F., Obermann, S., von Wasielewski, R., Haile, L., Manns, M.P., Korangy, F., and Greten, T.F. (2009). Increase in frequency of myeloid-derived suppressor cells in mice with spontaneous pancreatic carcinoma. Immunology *128*, 141–149.

Appendix

Appendix A: Videos

Time Lapse microscopy videos referred to in the thesis can be found in this link. For description of each movie, refer to “List of videos”.

Appendix B: Supplementary Figures

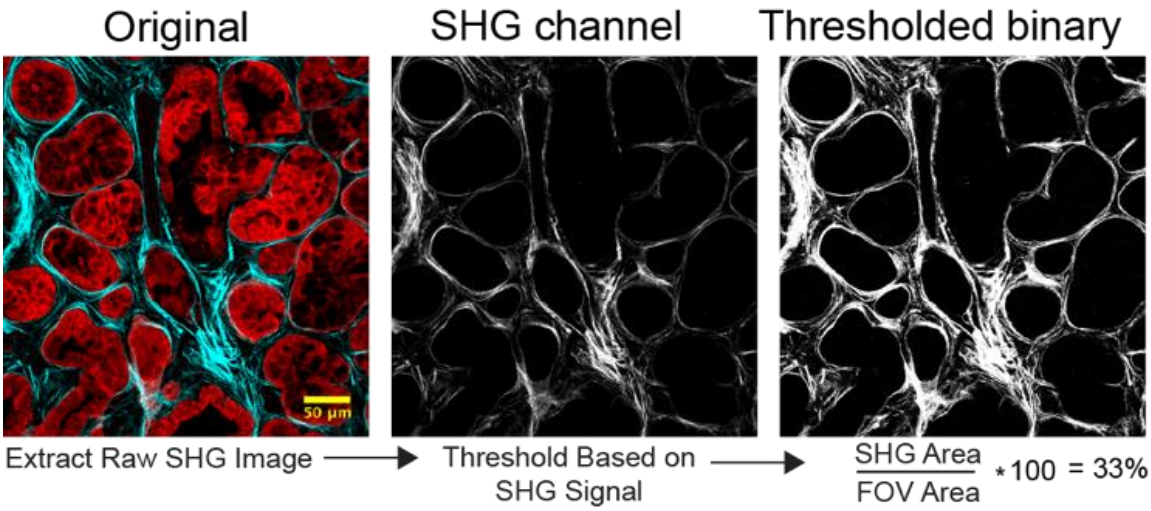

Supplementary Figure 1: Quantification of collagen in murine PDA. Example of fibrous collagen quantification, using Matlab, from a *KPCY* sample. Image illustrates YFP_+ carcinoma cells (pseudo colored red) from *KPCY* tissue and collagen fibers (cyan, left, and grey/white, middle and right). Scale bar = 50 µm. Figure panels extracted from Ray et al., submitted.

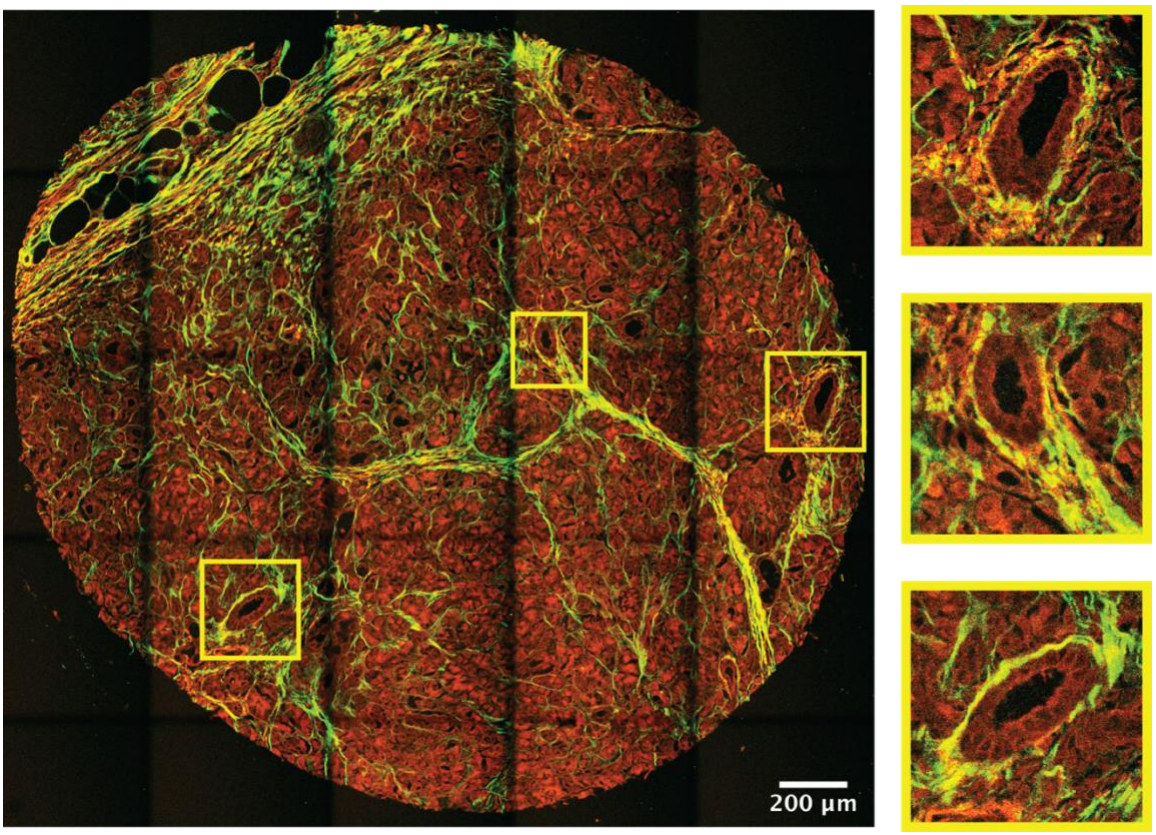

Supplementary Figure 2: Imaging of collagen architecture in human chronic pancreatitis. Atlas imaging of whole human chronic pancreatitis biopsy samples, from tissue microarray, for quantification of collagen signatures. Endogenous whole tissue fluorescence is pseudo colored red and collagen SHG is pseudo colored greenish-yellow. Right panels show magnified views of sample insets showing fibrous collagen patterns around ductal structures enclosed by the yellow box. Scale bar = 200 µm.

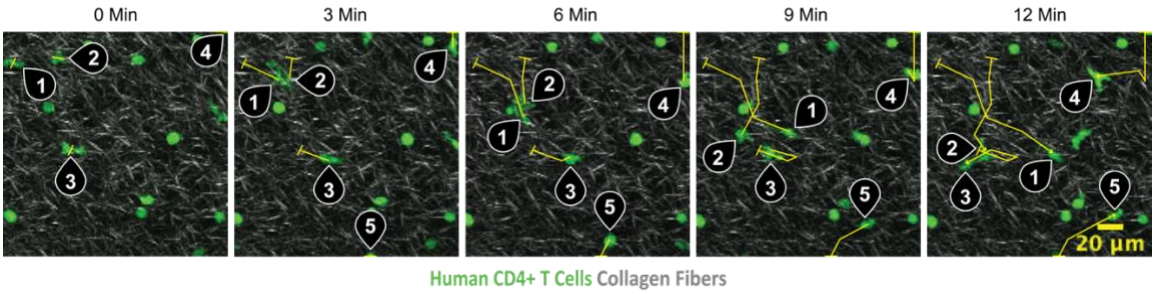

Supplementary Figure 3: Sample sequence of hCD4+ T cell migration in 3D collagen-FN matrices. Imaging sequence of hCD4+ T cell migration in 3D collagen-FN matrices. Sample migration tracks of individual T cells are highlighted using numerated pins along with their tracks (yellow curves; *start position - tick, end position - arrowhead*). Images are magnified MIPs of a 75 µm z-stack. Scale bar = 20 µm.

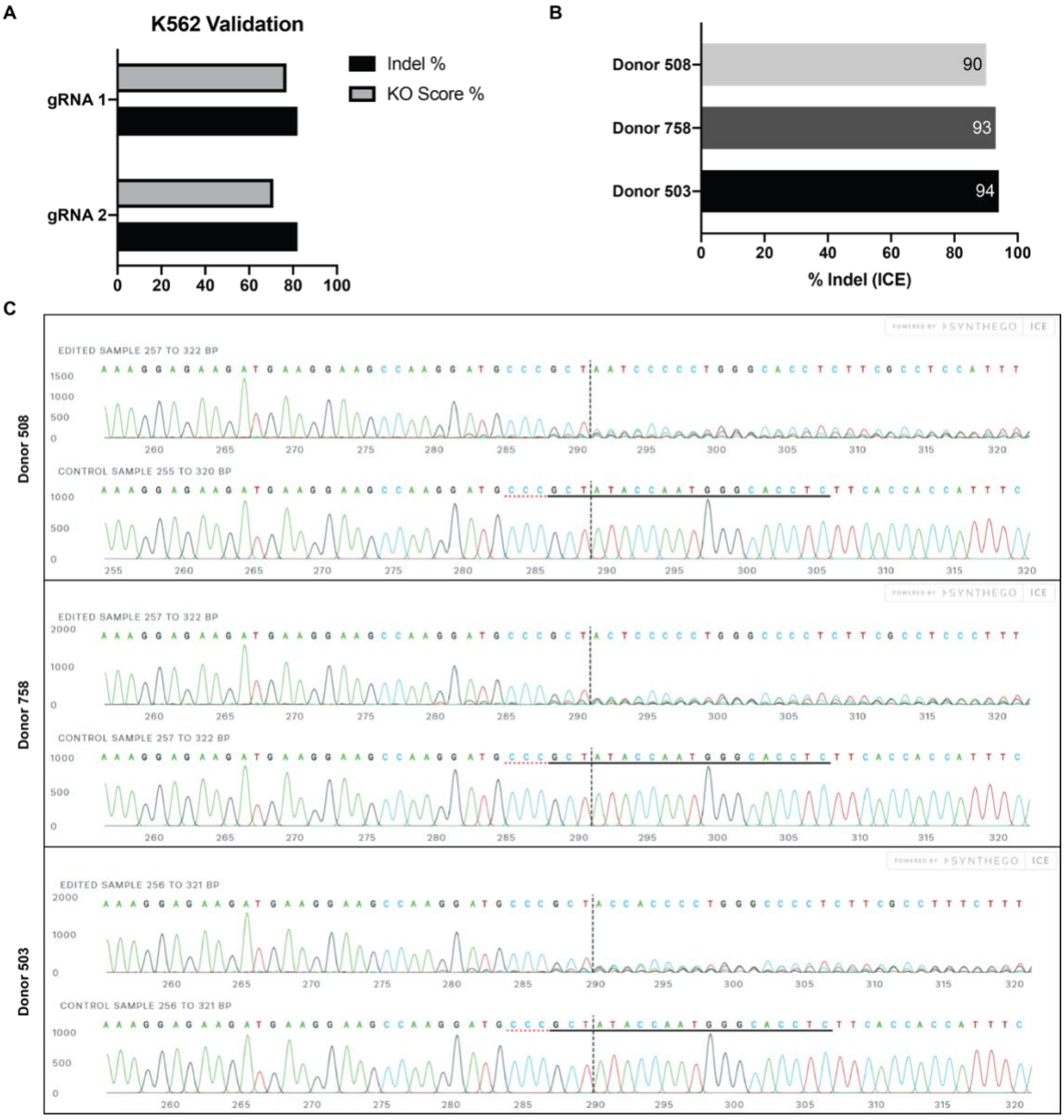

Supplementary Figure 4: Validation and genotyping of hGEF-H1 KO in human cells. (**A**) Validation of two hARHGEF2 gRNAs (Sequence 1: 5'-GAGGUGCCCAUUGGUAUAGC -3' and sequence 2: 5'-GGAGAAGATGAAGGAAGCCA-3'), in K562 cells, with corresponding Indel and KO score %. (**B**) Indel % of hGEF-H1 KO in three donors of hCD4+ T cells utilizing validated gRNA (A) based on KO score %. (**C**) Sanger sequence view showing edited and wild-type (control) sequences in the region around the guide sequence. The hARHGEF2 gRNA 1 sequence is 5'-GAGGTGCCCATTGGTATAGC-3' while the horizontal black underlined region represents the reverse complementary guide sequence. The horizontal red underline is the PAM site while the PAM CRISPR/Cas-9 recognition sequence is GGG. The vertical black dotted line represents the actual cut site. Tabdanov and Rodriguez-Merced et al., submitted.